# Ocean Acidification trends and Carbonate System dynamics across the North Atlantic Subpolar Gyre water masses during 2009-2019

David Curbelo-Hernández[1], Fiz F. Pérez[2], Melchor González-Dávila[1,*], Sergey V. Gladyshev[3], Aridane G. González[1], David González-Santana[1], Antón Velo[2], Alexey Sokov[3], and J. Magdalena Santana-Casiano[1].

[1] Instituto de Oceanografía y Cambio Global (IOCAG), Universidad de Las Palmas de Gran Canaria (ULPGC). Las Palmas de Gran Canaria, Spain.

[2] Instituto de Investigaciones Marinas (IIM), CSIC, Vigo, Spain.

[3] P. P. Shirshov Institute of Oceanology, Russian Academy of Sciences, Moscow, Russian Federation

*Corresponding Author: Melchor González-Dávila (melchor.gonzalez@ulpgc.es)

**Keypoints:**

During the 2010s, the subpolar North Atlantic experienced a 50-86% increase in anthropogenic $CO_2$, accelerating by 7-10% the acidification.

Anthropogenic $CO_2$ contributed to acidification by 53-68% in upper layers and >82% in the interior ocean.

The acidification trends (0.0006 and 0.0032 units $yr^{-1}$) declined the $\Omega_{Ca}$ and $\Omega_{Arag}$ by 0.004-0.021 and 0.003-0.0013 units $yr^{-1}$, respectively.

20 **Abstract**

21 The $CO_2$-carbonate system dynamics in the North Atlantic Subpolar Gyre (NASPG) were
22 evaluated between 2009 and 2019. Data was collected aboard eight summer cruises through
23 the CLIVAR 59.5ºN section. The Ocean Acidification (OA) patterns and the reduction in the
24 saturation state of calcite ($\Omega_{Ca}$) and aragonite ($\Omega_{Arag}$) in response to the increasing
25 anthropogenic $CO_2$ ($C_{ant}$) were assessed within the Irminger, Iceland and Rockall basins
26 during a poorly-assessed decade in which the physical patterns reversed in comparison with
27 previous well-known periods. The observed cooling, freshening and enhanced ventilation
28 increased the interannual rate of accumulation of $C_{ant}$ in the interior ocean by 50-86% and
29 the OA rates by close to 10%. The OA trends were 0.0013-0.0032 units $yr^{-1}$ in the Irminger
30 and Iceland basin and 0.0006-0.0024 units $yr^{-1}$ in the Rockall Trough, causing a decline in
31 $\Omega_{Ca}$ and $\Omega_{Arag}$ of 0.004-0.021 and 0.003-0.0013 units $yr^{-1}$, respectively. The $C_{ant}$-driven rise
32 in total inorganic carbon ($C_T$) was the main driver of the OA (contributed by 53-68% in upper
33 layers and >82% toward the interior ocean) and the reduction in $\Omega_{Ca}$ and $\Omega_{Arag}$ (>64%). The
34 transient decrease in temperature, salinity and $A_T$ collectively counteracts the $C_T$-driven
35 acidification by 45-85% in the upper layers and in the shallow Rockall Trough and by <10%
36 in the interior ocean. The present investigation reports the acceleration of the OA within the
37 NASPG and expands knowledge about the future state of the ocean.

38 **Keywords:** Ocean Acidification, Anthropogenic Carbon, North Atlantic Subpolar Gyre.

## 1. Introduction

The ocean uptake of approximately one-third of the $CO_2$ released into the atmosphere (Friedlingstein et al., 2023; Gruber et al., 2019a) has an important role in the climate regulation causing changes in the marine carbonate chemistry. The exponential increase in the global ocean $CO_2$ sink in phase with those of anthropogenic emissions (Friedlingstein et al., 2023) has resulted in a long-term decrease in the concentration of carbonate ions ($[CO_3^{2-}]$) and pH. This process has been collectively referred to as Ocean Acidification (OA; Caldeira and Wickett, 2005, 2003; Doney et al., 2009; Orr et al., 2005; Raven et al., 2005; Feely et al., 2009) and favour the dissolution of calcium carbonate ($CaCO_3$). It affects not only calcifying marine organisms and ecosystems which use the biogenic $CaCO_3$ forms of calcite and aragonite (e. g. Gattuso et al., 2015; Langdon et al., 2000; Pörtner et al., 2004, 2019; Riebesell et al., 2000) but also the global biogeochemical cycles (Gehlen et al., 2011; Matear and Lenton, 2014).

The absorption of anthropogenic $CO_2$ has reduced the pH of the global surface ocean by 0.1 units since preindustrial times, representing approximately a 30% increase in acidity (Caldeira and Wickett, 2003). According to the IPCC's Representative Concentration Pathways (RCPs) scenarios (Van Vuuren et al., 2011; Moss et al., 2010), which project various future trajectories of greenhouse gas concentrations, the model projections estimate a potential pH decrease of 0.3–0.4 units by the end of the century under the RCP8.5 scenario, which assumes continued high $CO_2$ emissions. In contrast, the most conservative RCP2.6 scenario, which includes significant emission reductions, anticipates a pH drop of 0.2–0.3 units (IPCC 2013 and 2021). However, as the absorption and storing of anthropogenic carbon ($C_{ant}$), defined as the fraction of inorganic carbon resulted from human emissions (Sarmiento et al., 1992), is not uniform within the ocean (Sabine et al., 2004a), OA rates may show a significant spatial variability and should be regionally studied. The temporal evolution of the carbonate system variables in surface waters are monitored and assessed in several time-series stations located across different ocean regions (Bates et al., 2014). The largest OA rates are expected to occur across high northern and southern latitudes (Bellerby et al., 2005; Orr et al., 2005), where deep convective overturning and subduction occur favouring the entrance of $C_{ant}$ in the interior ocean (Maier-Reimer and Hasselmann, 1987; Lazier et al., 2002; Sarmiento et al., 1992).

The North Atlantic is one of the strongest $CO_2$ sinks and stores over 25% of the $C_{ant}$ accumulated in the global ocean (e. g. Gruber et al., 2019; Khatiwala et al., 2013; Pérez et al., 2024, 2010, 2008, 2024; Sabine et al., 2004; Takahashi et al., 2009). The Atlantic Meridional Overturning Circulation (AMOC) plays a significant role by conveying acidified $C_{ant}$-loaded waters polewards and exporting them to the ocean interior across deep-water formation areas (Lazier et al., 2002; Pérez et al., 2013, 2008; Steinfeldt et al., 2009). It contributes to homogenize the $C_{ant}$ and pH in the whole water column in such regions and exported these properties southwards to the global deep ocean (Perez et al., 2018). Thus, the North Atlantic behaves as a crucial region for understanding the impacts of anthropogenic forcing on the global ocean.

OA has been widely studied in the North Atlantic through the monitoring of the ocean physicochemical properties at time-series stations (summarized by Bates et al., 2014) placed in subtropical and subpolar latitudes: the European Station for Time series in the Ocean at the Canary Islands (ESTOC; 29.04ºN, 15.50ºW; González-Dávila et al., 2010; González-Dávila and Santana-Casiano, 2023; Santana-Casiano et al., 2007), the Bermuda Atlantic Time-series Study (BATS; 32.0ºN, 64.0ºW; Bates et al., 2012), the Irminger Sea Time Series (IRM-TS; 64.3ºN, 28.0ºW; Olafsson et al., 2010) and the Iceland Sea Time Series (IS-TS; 68.0ºN, 12.66ºW; Olafsson et al., 2009, 2010). OA rates has also been evaluated along transects through repeated hydrographic cruises (i.e. Guallart et al., 2015; García-Ibáñez et al., 2016; Vázquez-Rodríguez et al., 2012b) or even covered by volunteer observing ships (Fröb et al., 2019). These investigations have revealed a rate of decrease in pH of ~0.001-0.002 units $yr^{-1}$. Moreover, González-Dávila and Santana-Casiano (2023) has recently indicated that these rates are increasing since 1995.

The assessment of OA is of especial interest across the North Atlantic Subpolar Gyre (NASPG; 50-60ºN), where the atmospheric $CO_2$ sink is particularly strong and the deep-water formation processes favour the storage of $C_{ant}$ through the whole water column (Gruber et al., 2019b; Sabine et al., 2004b; Watson et al., 2009, Pérez et al. 2008). Likewise, the deep-water formation processes create the largest and deepest ocean environments supersaturated for aragonite (at more than 2000 m depth; Feely et al., 2004; Jiang et al., 2015), which is the main $CaCO_3$ mineral for Cold-water corals (CWC; Roberts et al., 2009) and some pteropods

98  (Bathmann et al., 1991; Urban-Rich et al., 2001). These deep biomes are predicted to be one

99  of the first in the global ocean affected by OA, mainly due to the shoaling of the Aragonite

100 Saturation Horizon and its progressive exposition to undersaturated conditions for aragonite at

101 intermediate and deep waters (Gehlen et al 2014; Guinotte et al., 2006; Raven et al., 2005;

102 Roberts et al., 2009; Turley et al., 2007).

103 The physical processes along the NASPG, which are subject to significant spatiotemporal

104 variability introduced by the atmospheric forcing and climatology on an interannual scale,

105 directly influenced the biogeochemistry (Corbière et al., 2007; Fröb et al., 2019). The changes

106 in North Atlantic Current (NAC) modifies the poleward heat transport from subtropical

107 latitudes and the air-sea interactions, influencing temperature patterns (Josey et al., 2018;

108 Mercier et al., 2015). Recent studies noticed the surface cooling and freshening of the NASPG

109 in the 2010s (Holliday et al., 2020; Josey et al., 2018; Robson et al., 2016; Tesdal et al., 2018)

110 contrasting with the period of warming and salinification in the 1990s extended until 2005

111 (Häkkinen and Rhines, 2004; Hátún et al., 2005; Robson et al., 2014). Anomalously heat loss

112 and winter deep convection were found to be of high intense since 2008 contributing to the

113 extreme cold anomaly along the NASPG (e. g. De Jong et al., 2012; de Jong and de Steur,

114 2016; Fröb et al., 2019, 2016; Gladyshev et al., 2016b, 2016a; Piron et al., 2017; Våge et al.,

115 2009). These fluctuations in the vertical mixing and ocean circulation patterns introduces

116 changes in the distribution of the carbonate system variables.

117 The estimated OA trend over 1991-2011 for surface waters across the North Atlantic Subpolar

118 biome was $-0.0020 \pm 0.0001$ units yr$^{-1}$ (Lauvset et al., 2015). Chau et al., 2024 recently reported

119 that the surface waters in the Irminger and Iceland basins has acidified over 1985-2021 at rates

120 of $-0.0016 \pm 0.0001$ and $-0.0014 \pm 0.0001$ units yr$^{-1}$. Several observation-based investigations

121 have evaluated the drivers, trends and impacts of OA through the entire water column in the

122 Irminger and Iceland basins (e. g. Fontela et al., 2020; García-Ibáñez et al., 2021, 2016; Perez

123 et al., 2018; Pérez et al., 2021; Ríos et al., 2015), while few studies have addressed it in the

124 Rockall Trough (e. g. McGrath et al., 2013, 2012a, 2012b, Humphreys et al., 2016) due to lack

125 of repeated hydrographic sections or time-series stations and subsequent limitation of

126 continuous surface-to-bottom data. The high longitudinal variability in the NASPG caused by

127 the influence of different circulation patterns and water masses (García-Ibáñez et al., 2018,

2015) introduced several physicochemical heterogeneities between the Irminger and Iceland with the Rockall basin (Ellett et al., 1986; McGrath et al., 2013, 2012b; Holliday et al., 2000). These differences in the distributions of Marine Carbonate System (MCS) variables should be considered to improve our understanding of OA in the entire North Atlantic.

This study evaluated the OA in the NASPG across the Irminger, Iceland and Rockall basins during the 2010s. High-quality direct measurements of $CO_2$ system variables from eight hydrographic cruises occupying 59.5ºN between 2009 and 2019 were used to evaluate the drivers and trends of pH, and the potential effects of OA on calcifying organisms of changes in calcite ($\Omega Ca$) and aragonite ($\Omega Ar$) saturation states. This study advances our understanding of the complexities associated with OA in the NASPG and supports ongoing efforts to model and predict future acidification scenarios in the North Atlantic and global ocean.

## 2. Methodology

### 2.1. Data collection

Data were collected from eight summer cruises conducted along the transverse hydrographic section at 59.5ºN between 2009 and 2019 (Daniault et al., 2016; Gladyshev et al., 2016b, 2017, 2018; Sarafanov et al., 2018). This section is part of the World Climate Research Programme (WCRP) within the framework of the CLIVAR (Climate and Ocean: Variability, Predictability and Change) project and covers the length of the Subpolar North Atlantic between Scotland and Greenland (4.5-43.0ºW), crossing the Irminger and Iceland basins and the Rockall Trough (Figure 1). Generally, the sampling stations were equidistantly spaced every 20 nmi apart (~1/3º longitude) and repeated in all the cruises except for the cruise of 2016, when the station spacing was decreased to 10 nmi over Reykjanes Ridge western and eastern slopes. The distance between stations over the east Greenland slope and shelf always decreased from 10 nmi to about 2 nmi. The surface-to-bottom sampling and in situ measurements were performed by using a SBE 911plus CTD with SBE32 Carousel containing 24 Niskin bottles (10 L) with additional sensors for pressure (P), dual temperature (T) and salinity (S), and dissolved oxygen (DO). The eight cruises included in the new dataset are the result of an international collaboration between researchers from the P. P. Shirshov Institute of Oceanology at the Russian Academy of Science and the Marine Chemistry research group from the

157 Oceanography and Global Change Institute (QUIMA-IOCAG) at the University of Las Palmas

158 de Gran Canaria (ULPGC). A detailed overview of the cruises is given in Table 1.

### 2.1.1. $CO_2$ system variables measurements

160 The analysis of the MCS variables followed the same analytical methodology and provided

161 high-quality $CO_2$ measurements in all the hydrographic cruises. It includes the sampling and

162 data collection techniques, quality control and calculation procedures published in the updated

163 version of the DOE method manual for $CO_2$ analysis in seawater given by Dickson et al., 2007.

164 The seawater samples were onboard analysed for total alkalinity ($A_T$) and total inorganic

165 carbon ($C_T$) determination by using a VINDTA 3C and following Mintrop et al., (2000). The

166 $A_T$ was analysed by potentiometric titration with HCl to the carbonic acid endpoint and

167 determined through the developing of the full titration curve (Millero et al., 1993; Dickson and

168 Goyet, 1994). The $C_T$ was determined through coulometric titration (Johnson et al., 1993). The

169 VINDTA 3C was calibrated through the titration of Certified Reference Material (CRMs;

170 provided by A. Dickson at Scripps Institution of Oceanography), giving values with an

171 accuracy of $\pm 1.5$ $\mu$mol kg$^{-1}$ for $A_T$ and $\pm 1.0$ $\mu$mol kg$^{-1}$ for $C_T$.

172 Spectrophotometric pH measurements (Clayton and Byrne, 1993) in total scale at constant

173 temperature of 15ºC ($pH_{T,15}$) were performed for the cruises between 2009 and 2016. A

174 spectrophotometric pH sensor (SP101-SM) developed by the QUIMA-IOCAG group at the

175 ULPGC in collaboration with SensorLab (González-Dávila, 2014; González-Dávila et al.,

176 2016) was used. The method uses 4 wavelengths analysis for pH indicator dyes (m-cresol

177 purple), includes auto-cleaning steps and performs a blank for pH calculation immediately

178 after the dye injection. The spectrophotometric sensor was *in situ* tested by using a TRIS

179 seawater buffer (Ramette et al., 1977) and provided $pH_{T15}$ values with an accuracy of $\pm 0.002$

180 units. To account for the systematic uncertainty reported by DelValls and Dickson (1998)

181 related to the pK* values of m-cresol purple, and in line with their recommendations, a

182 correction of +0.0047 units was applied to the measured $pH_{T15}$. This adjustment ensures that

183 the calculated pH values are consistent with the more accurate pK* determinations.

### 2.1.2. Dissolved oxygen (DO) measurements

The WINKLER method introduced by Winkler (1888) and optimized by Carpenter (1965) and Carrit and Carpenter (1966) was used to analytically determine the dissolved oxygen (DO) of the seawater samples in all the cruises from 2009 to 2016. The seawater samples for DO determination were collected from the bottle samples in pre-calibrated glass wide-neck bottles avoiding bubble formation. The temperature of the water was recorded during the sampling. All the reagents and solutions used for dissolved oxygen determination were prepared following the procedures described by Dickson, (1995) and their possible impurities were controlled by determining a blank every 2 days.

As DO could not be analytically measured during the cruise of 2019 (due to limitations related with the oceanographic cruise plan), it was computed for this year by comparing the performance of the DO sensor during the cruise of 2019 versus (1) DO data estimated by a neural network for the cruises of 2016 and 2019 and (2) WINKLER-measured DO data in the cruise of 2016. The neural network ESPER_NN (Empirical Seawater Property Estimation Routine) introduced by Carter et al., (2021) was used for DO estimations. The computational procedure is detailed in Appendix A.

## 2.2. Data processing

### 2.2.1. Evaluation of the internal consistency of the data using CANYON-B

The measured and determined data were compared with estimations given by the Bayesian neural network "CANYON-B" (Bittig et al., 2018), a re-developed and more robust neural network based on CANYON (CArbonate system and Nutrients concentration from hYdrological properties and Oxygen using a Neural-network; Sauzède et al., 2017). CANYON-B estimates the four MCS variables ($A_T$, $C_T$, pH and $pCO_2$) and macronutrients concentrations ($PO_4^{3-}$, $NO_3^-$ and $Si(OH)_4$, hereinafter $PO_4$, $NO_3$ and $Si(OH)_4$) as a function of a simple set of input variables which include P, T, S, DO, latitude, longitude and date. This neural network is trained on and validated against bottle data from GLODAPv2 and recent GO-SHIP profiles and compared with sensor data from Argo floats. The standard errors of estimate reported for CANYON-B by Bittig et al., (2018) are 6.3 µmol kg$^{-1}$ for $A_T$, 7.1 µmol kg$^{-1}$ for $C_T$, 0.013 units for pH, 20 µatm for $pCO_2$, 0.051 µmol kg$^{-1}$ for $PO_4$, 0.68 µmol kg$^{-1}$ for $NO_3$ and 2.3 µmol kg$^{-1}$ for $Si(OH)_4$. The crossover analysis between measured and estimated data did not show systematic differences but individual outliers. The measured data that were

215 higher/lower than the CANYON-B estimate by plus/minus twice the predicted variable
216 uncertainty of the neural network was considered as outliers and removed from the dataset.

217 The total amount of measured data was 8974 for $A_T$, 7495 for $C_T$, 8706 for $pH_{T,15}$, 9656 for
218 DO, 9114 for $PO_4$ and 9192 for $Si(OH)_4$. The difference between the measured and CANYON-
219 B-estimated variables (referred hereinafter as canyon-estimated variables) were performed for
220 each sample in which CANYON-B could be applied (samples with availability of T, S and DO
221 measurements). The number of data, mean values and standard deviation of the measured
222 variables for each cruise were summarized in Table S1. The average differences with the 95%
223 confidence interval for each cruise are shown in Table S2. The average differences for the
224 entire period (2009-2019) were lower than 2.1 µmol kg$^{-1}$ for $A_T$, 2 µmol kg$^{-1}$ for $C_T$, 0.0002 for
225 pH, 0.02 µmol kg$^{-1}$ for $PO_4$ and 0.25 µmol kg$^{-1}$ for $Si(OH)_4$. The minimal difference between
226 the measured and canyon-estimated pH infers confidence in the correction applied to the
227 measured pH following DelValls and Dickson (1998).

### 228    2.2.2.  Computational methods

229 The computational procedures to calculate MCS system variables applied in this investigation
230 used the $CO_{2,SYS}$ programme developed by Lewis and Wallace, (1998) and run with the
231 MATLAB software (van Heuven et al., 2011; Orr et al., 2018; Sharp et al., 2023). The set of
232 constants used for computations includes the carbonic acid dissociation constants of Lueker et
233 al., (2000), the $HSO_4^-$ dissociation constant of Dickson, (1990), the HF dissociation constant
234 of Perez and Fraga, (1987) and the value of $[B]_T$ determined by Lee et al., (2010). The pH in
235 total scale at *in situ* temperature ($pH_T$) was computed from the measured $A_T$ and $pH_{T,15}$ (the
236 computed $C_T$ was given as an output). The $pH_T$ for the cruise of 2019, in which direct pH
237 measurements were not performed, was computed from the measured $A_T$ and $C_T$.

238 The saturation states of Calcite ($\Omega_{Ca}$) and Aragonite ($\Omega_{Arag}$), determined from the product of
239 the ion concentrations of calcium ($[Ca^{2+}]$) and carbonate ($[CO_3^{2-}]$) divided by the stoichiometry
240 solubility products ($K_{sp}$) for calcite ($K_{Ca}$) and aragonite ($K_{Arag}$) given by Mucci (1983), were
241 generated as outputs of the $CO_{2,SYS}$ computational routine. The decrease in $\Omega_{Ca}$ and $\Omega_{Arag}$
242 reports the adverse impacts of OA on marine calcification processes (e. g. Gattuso et al., 2015;
243 Langdon et al., 2000; Pörtner et al., 2004, 2019; Riebesell et al., 2000).

244 An internal consistency test was conducted on the three measured MCS variables. The

245 measured variables were compared with canyon-estimated and $CO_{2SYS}$-computed variables.

246 The average differences and standard deviations were summarized in Table S2 and ensure the

247 consistency of the observations. In addition, due to gaps in data, an intercomparison between

248 measured and computed $C_T$ and $pH_{T15}$ was performed. It considers the availability of

249 measurements for each latitude, longitude and time and the differences between the measured

250 and computed pH with the canyon-estimated $pH_T$. The use of measured or computed $C_T$

251 followed these conditions: (1) If there is measured $C_T$ but not measured pH, measured $C_T$ was

252 used, (2) if there is measured pH but not measured $C_T$, computed $C_T$ was used, (3) and if there

253 is measured $C_T$ and pH, measured $C_T$ was used when the differences between measured and

254 canyon $pH_T$ is lower than the differences between computed and canyon-estimated $pH_T$, while

255 computed $C_T$ was used when the opposite happens. In total, 6375 measured and 2872 computed

256 $C_T$ data were used in this study (69% and 31%, respectively). The average differences in each

257 cruise between the combined (measured and computed, also referred as "$C_{T\,(new)}$") and canyon-

258 estimated $C_T$ variable is provided in Table S2. The amount and percentage of measured and

259 computed $C_T$ data per cruise is given in Table S3. As the measured $C_T$ was in average 1.9 µmol

260 $kg^{-1}$ higher than the canyon-estimated and the computed $C_T$ was in average 1.7 µmol $kg^{-1}$ lower,

261 the new compilation based on these previous conditions allowed to reduce the difference to

262 1.5 µmol $kg^{-1}$.

263     **2.2.3. Anthropogenic $CO_2$ ($C_{ant}$) calculation**

264 The anthropogenic $CO_2$ ($C_{ant}$) was estimated by using the biogeochemical back-calculation

265 $\phi C_T^o$ method, which has an overall estimated uncertainty of $\pm 5.2$ µmol $kg^{-1}$ (Pérez et al., 2008;

266 Vázquez-Rodríguez et al., 2009). The method considers the change of $C_T$ between the

267 preindustrial era (1750) and the time of the observations, as well as the processes involved in

268 the uptake and distribution of $C_{ant}$ (biogeochemistry, mixing processes and air-sea fluxes). The

269 $C_{ant}$ was calculated (Eq. 1) as the difference between the $C_T$ at the time of observation, the $C_T$

270 that the seawater would have in equilibrium with a preindustrial atmosphere (preformed $C_T$;

271 $C_T^{pre}$), the offsets of such equilibrium values (air-sea $CO_2$ disequilibrium; $\Delta C_T^{dis}$) and the

272 changes in $C_T$ due to the organic and carbonate pumps ($\Delta C_T^{bio}$). The $C_T$ and $A_T$ at the time of

273 observations and the preformed $A_T$ ($A_T^0$) are needed as input parameters and the computational

274 procedure was described by Vázquez-Rodríguez et al., (2012).

$$C_{ant} = C_T - C_T^{pre} - \Delta C_T^{dis} - \Delta C_T^{bio} \tag{1}$$

276 The $\phi C_T^o$ method is an improved process-based $C_{ant}$ estimation method tested and widely

277 applied in the Atlantic Ocean (Vázquez-Rodríguez et al., 2009) which present distinctive

278 characteristics relative to existing $C_{ant}$ approaches, such as the classical $\Delta C^*$ (GSS' 96; Gruber

279 et al., 1996) and the TrOCA (Touratier et al., 2007). The main advantages of the $\phi C_T^o$ method

280 has been described by Pérez et al., (2008).

### 281 **2.2.4. Hydrographic characterization**

282 The characterization of the basins and water masses was done by considering the 2009-2019

283 mean combined 59.5ºN section constructed with potential vorticity, dissolved oxygen and

284 salinity together with the large-scale circulation in the North Atlantic (e. g. Lherminier et al.,

285 2010; Pérez et al., 2021; Sarafanov et al., 2012; Schmitz and McCartney, 1993; Schott and

286 Brandt, 2007; Sutherland and Pickart, 2008). A schematic diagram with the main surface and

287 deep currents in the NASPG is depicted in Figure 1a. The basin division considered the NAC

288 pathways and revealed a west-to-east distribution comprising the Irminger and Iceland basins

289 and the Rockall Trough. The Iceland basin was delimited along its eastern boundary by the

290 central NAC branches around the northern part of the Haton Bank and George Bligh Bank,

291 and along its western boundary by the Return Current over the eastern flank of the Reykjanes

292 Ridge slope. This suggest that the Iceland basin could be longitudinally separated in two

293 subregions: the western Iceland basin (24.0-29.5ºW) and the eastern Iceland basin (14.0-

294 24.0ºW).

295 The upper layers were mainly occupied by Subpolar Mode Waters (SPMW) and North Atlantic

296 Central Waters (NACW). SPMW is formed in the Iceland basin (McCartney and Talley, 1982;

297 Brambilla and Talley, 2008; Tsuchiya et al., 1992; Van Aken and Becker, 1996), flow eastward

298 to the Rockall Trough and recirculate across the Reykjanes Ridge (Brambilla and Talley, 2008).

299 In the Irminger basin, SPMW flow with the Irminger Current to the north over the western

300 Reykjanes Ridge flank and to the south over the eastern Greenland slope (Figure 1a). Thus,

301 SPMW signal was detected in the western and eastern Irminger basin up to 400-700 m depth

and limited to subsurface depths in the central part of the basin. NACW were placed above SPMW east of the Irminger basin and separated in two branches: Eastern North Atlantic Central Water (ENACW), formed by winter convection in the intergyre region and moved poleward from the Bay of Biscay through the Rockall Trough (Harvey, 1982; Pollard et al., 1996), and Western North Atlantic Central Water (WNACW), flowing northward with the NAC along the western Iceland basin. The intermediate layers were mainly occupied by Labrador Sea Water (LSW), formed in the Labrador Sea and transported eastward (e. g. Pickart et al., 2003; Fröb et al., 2016). LSW path diverges into two cores when it reaches the Reykjanes Ridge (Álvarez et al., 2004; Pickart et al., 2003): a fraction of LSW rapidly moved to the Irminger basin and incorporated into the Deep Western Boundary Current (DWBC) (Bersch et al., 2007) and a second LSW core was transported eastward into the Iceland and Rockall basins. In the Irminger and western Iceland basin, LSW placed above Iceland-Scotland Overflow Water (ISOW), which originated from the overflow of Norwegian Sea waters over the Iceland–Scotland ridges and flowed southward and below 1500 m depth through the western NASPG (van Aken and de Boer, 1995; Dickson et al., 2002; Fogelqvist et al., 2003). The bottom of the western Irminger basin was occupied by Denmark Strait Overflow Water (DSOW), recently formed from deep waters from the Nordic seas flowing southward over the Greenland-Iceland ridge and sinking through the eastern Greenland slope (Read, 2000; Stramma et al., 2004; Yashayaev and Dickson, 2008). LSW core transported eastwards rises in depth through the western Haton Bank flank and occupy the bottom depths in the eastern Iceland basin and in the Rockall Trough. A low-ventilated thermocline layer is placed between SPMW and LSW in the eastern NASPG (García-Ibáñez et al., 2016), which represent the product of mixing with waters coming from the south (i. e. Mediterranean Waters; MW).

To enhance the comprehension of the spatial distribution and trends of the biogeochemical variables and to facilitate comparisons with previous studies along the NASPG, the hydrographic characterization was simplified based on the following principles: (1) the Iceland basin was not divided into its western and eastern parts and its longitudinal span was delimited by the Reykjanes Ridge (29.5ºW) and the Haton Bank (17ºW), (2) upper Labrador Sea Water (uLSW) was separated from deeper LSW (e. g. Stramma et al., 2004), (3) the weak and spatially-limited influence of the return current and WNACW was removed by considering the upper and intermediate layers of both the Irminger and Iceland basin fully occupied by SPMW

above uLSW, and (4) only the east branch of NACW (ENACW), placed above SPMW, was contemplated for the upper Rockall Trough.

The whole water column was separated in layers delimited by potential density isopycnals at a reference pressure of 0 dbar following Azetsu-Scott et al. (2003), Kieke et al. (2007), Pérez et al. (2008) and Yashayaev et al. (2008). The vertically distributed water masses separated in density layers is represented for the entire section in Figure 1b. The vertical characterization in density layers allows to consistently compare the low-variable physical and chemical properties within each water mass, enabling to assume linearity in the ocean $CO_2$ system. The determination of the isopycnal limits between layers in the Irminger and Iceland basins followed previous biogeochemical studies in the western boundary of the North Atlantic (Fontela et al., 2020; García-Ibáñez et al., 2016; Pérez et al., 2010, 2008; Vázquez-Rodríguez et al., 2012a). The surface-to-bottom distribution of the main water masses in these basins (with their respective $\sigma_0$ lower limits shown in brackets) was SPMW (27.68 kg m$^{-3}$), uLSW (27.76 kg m$^{-3}$), LSW (27.81 kg m$^{-3}$) and ISOW (27.88 kg m$^{-3}$). The low temperature and salinity DSOW were considered at the bottom of the westernmost part of the Irminger basin. The hydrography of the Rockall Trough has been characterized in previous studies in the Northeast Atlantic (e. g. Ellett et al., 1986; Harvey, 1982; McGrath et al., 2012a, 2012b; Holliday et al., 2000), with the main water masses surface-to-bottom distributed as ENACW (27.35 kg m$^{-3}$), SPMW (27.68 kg m$^{-3}$) and LSW (bottom).

### 2.2.5. Data adjustment for trends computation

The interannual trends were analysed through the whole water column across the Irminger, Iceland and Rockall basins by yearly averaging the variables for each layer, following previous studies in the NASPG (e.g. Fontela et al., 2020; García-Ibáñez et al., 2016). Linear regressions were applied to the mean values, in which the value of the slope give the ratios of interannual changes. The errors of the means were calculated through the relation of the Standard Deviation and the square root of the number of bottle samples in each layer and cruise ($Standard\ Deviation/\sqrt{n}$). The standard errors of the slopes were calculated by accounting for the error propagation of the annual mean values. The Pearson correlation test was employed to assess the strength and direction of the linear regressions and evaluate the significance of the interannual trends. This test provided correlation coefficients ($r^2$) and corresponding p-

values to determine statistical significance. The p-values $\leq 0.01$ indicated that the trends were statistically significant at the 99% confidence level, the p-values $\leq 0.05$ indicated that the trends were statistically significant at the 95% confidence level and the p-values $\leq 0.1$ indicated that the trends were statistically significant at the 90% level. Trends with p-values $> 0.1$ were considered as not statistically significant but provided an estimation of the temporal evolution of the variables in their respective layers. These not statistically significant trends were explained by the high variability and changes in the low-limit depth of the layers encountered between consecutive years.

As there was a lack of in situ measurements and sampling along the west half of the Irminger basin (36.5-42.5ºW) in the cruise of 2019 (due to permit restrictions to study the national waters of Denmark), the GO-SHIP A25-OVIDE data for the cruise of 2018 (available at SEANOE [https://www.seanoe.org/], Lherminier et al., 2022) were considered to adjust the 2019 data. The average values were calculated with both the available data in the easternmost part of the Irminger basin during the cruise of 2019 and the A25-OVIDE-2018 data available in the same part of the section (29.6-36.5ºW). The difference between these average values provides the variation of each variable from 2018 to 2019, which can be extrapolated to the western part of the Irminger basin by assuming linearity in the temporal evolution. Thus, the average values for 2019 were adjusted by applying the product with the calculated change between 2018 and 2019.

### 2.2.6. Deconvolution of the trends

OA trends arise due to the combined variations in T, S, $C_T$ and $A_T$. The influence of each driver on OA and subsequent impacts on marine calcification processes was analysed by assuming linearity and employing a first-order Taylor-series deconvolution (Sarmiento and Gruber, 2006) to evaluate the trends for $pH_T$ (Fröb et al., 2019; García-Ibáñez et al., 2016; Pérez et al., 2021; Takahashi et al., 1993; Tjiputra et al., 2014) and $\Omega$ (García-Ibáñez et al., 2021). The interannual rates of change of $pH_T$ and $\Omega$ result from the sum of their partial derivatives versus T, S, $C_T$ and $A_T$, calculated based on mean properties of each layer. The most recent equation defined by Pérez et al., (2021) was used (Eq. 2), in which $X$ represents $pH_T$, $\Omega_{Ca}$ and $\Omega_{Arag}$. and salinity-normalized $C_T$ and $A_T$ ($NC_T$ and $NA_T$, normalized to a constant salinity of 35) were used to remove the effect of the freshwater fluxes and evaporation/precipitation effects.

393
$$\frac{dX}{dt} = \frac{\partial X}{\partial T}\frac{dT}{dt} + \left(\frac{\partial X}{\partial S} + \frac{NC_T}{S_0}\frac{\partial X}{\partial C_T} + \frac{NA_T}{S_0}\frac{\partial X}{\partial A_T}\right)\frac{dS}{dt} + \frac{S}{S_0}\frac{\partial X}{\partial C_T}\frac{dNC_T}{dt} + \frac{S}{S_0}\frac{\partial X}{\partial A_T}\frac{dNA_T}{dt} \qquad (2)$$

394  It is important to remark that the changes in $NA_T$ and $NC_T$ are linked with biogeochemical

395  processes which have different influences: the processes involved in the organic carbon pump

396  contribute to strongly change the $NC_T$ weakly affecting the $NA_T$, while those involved in the

397  carbonate pump affect the $NA_T$ twice as much as $NC_T$. The complexity and heterogeneity of

398  the processes that govern the $pH_T$ change were considered by this equation.

### 3. Results

400  The vertical distribution of the physical and biogeochemical variables is depicted for the

401  cruises of 2009 and 2016 in Figures 2, 3, S2 and S3. The subsurface layers were characterized

402  by warmer and saltier waters than intermediate and deep layers among the three basins (Figure

403  2a and 2b). A West-to-East increase in temperature and salinity throughout the water column

404  was observed in all the cruises. The temperature and salinity signals were highest in the

405  Rockall Trough (4.5-11.0ºC and 35.0-35.4, respectively), followed by the Iceland basin (3.0-

406  7.5ºC and 34.9-35.2, respectively) and the Irminger basin (1.5-6.5ºC and 34.8-35.1,

407  respectively). The longitudinal differences in temperature were more remarkable toward the

408  upper layers through the SPMW and uLSW.

409  The spatial variability in the physical properties introduced heterogeneities in the distribution

410  of the $CO_2$ system variables. The $A_T$ show a well-correlated linear relationship with salinity

411  throughout the region ($A_T$ = 54.57 (±0.36) Salinity + 396.7 (± 12.7); $r^2$=0.90 and p-value <

412  0.01; Standard Error of Estimate of 2.9 µmol kg$^{-1}$), with lower and vertically-homogenized

413  average values in the Irminger basin (2302.8-2307.3 µmol kg$^{-1}$ in subsurface waters and

414  2298.8-2301.0 µmol kg$^{-1}$ in bottom waters) and Iceland basin (2308.7-2315.0 µmol kg$^{-1}$ in

415  subsurface waters and 2305.2-2308.0 µmol kg$^{-1}$ in bottom waters) compared to the Rockall

416  Trough (2317.9-2329.1 µmol kg$^{-1}$ in subsurface waters and 2308.5-2310.9 µmol kg$^{-1}$ in bottom

417  waters).

418  The upper layers were characterized by low $C_T$ values (2153.7-2160.8 µmol kg$^{-1}$ at the

419  Irminger basin, 2158.1-2168.4 µmol kg$^{-1}$ at the Iceland basin and 2120.1-2131.0 µmol kg$^{-1}$ at

420  the Rockall Trough), while a rapidly increment with depth was found below 100-200 m depth

421  (2154.7-2171.2 µmol kg$^{-1}$ throughout the section). The notable difference in the distribution of

422     $A_T$ and $C_T$ (Figure 2c and 3a, respectively) compared to those of $NA_T$ and $NC_T$ (Figure S2)

423     elucidated the remarkable significance of freshwater fluxes on the carbon variables

424     fluctuations during the period of study. The entrance of $C_{ant}$ through the atmosphere-seawater

425     interface caused higher $C_{ant}$ values in the upper layers (higher than 50 µmol kg$^{-1}$ in the first

426     1000 m depth; Figure 3b). The natural component of the $C_T$ ($C_{nat}=C_T-C_{ant}$; Figure 3c) correlated

427     with $C_T$ ($r^2=0.87$), and show a distribution characterized by low surface (<2110 µmol kg$^{-1}$) and

428     high bottom concentrations (>2130 µmol kg$^{-1}$).

429     The $pH_T$ (Figure 2d) rapidly decreased with depth showing the effect of biological uptake in

430     the upper layers and remineralization in deeper areas. The subsurface layer up to 100-200 m

431     depth exhibited $pH_T$ values higher than 8.025 units, which fell to 7.975 units at the bottom

432     layers. The $pH_T$ profiles reported an intrusion of remineralized and poorly oxygenated water

433     between 500 and 1000 m depth with relatively low $pH_T$ (<7.975) compared to adjacent layers

434     in the Iceland basin and in the western part of the Rockall Trough. This thermocline layer was

435     previously observed at ~500 m depth by García-Ibáñez et al., (2016) along a more meridional

436     transect which crossed the Iceland basin northwest-southeast. It introduces differences in the

437     intermediate water masses between the Iceland and Rockall basins with the Irminger basin.

438     The spatial and interannual fluctuations in the ventilation rates through changes in the water

439     mass formation and respiration processes represent a source of variability in the

440     biogeochemical patterns. The apparent oxygen utilization (AOU), defined as the difference

441     between saturated oxygen (calculated following Benson and Krause, 1984)  and measured

442     oxygen, was used to assess the ventilation of the water masses (Figure 2e). The high AOU

443     values indicate low ventilation, while low AOU values indicate the opposite. The slow renewal

444     of waters with high AOU favour the accumulation of the product of remineralization (de la

445     Paz et al. 2017). Thus, the areas with higher AOU (Figure 2e) were found to have high

446     concentration of $C_T$ and low $pH_T$ (Figures 3a and 2d, respectively). The near surface waters

447     permanently in contact with the atmosphere exhibited the lowest AOU values (<20 µmol kg$^{-1}$

448     ). The Irminger Basin presents the most significant water column ventilation among the entire

449     section, with maximum AOU ranging from 35 to 50 µmol kg$^{-1}$ at the LSW and ISOW and the

450     remarkable intrusion of oxygenated DSOW (>260 µmol kg$^{-1}$ DO) over the continental slope

451     with AOU ranging from 30 to 40 µmol kg$^{-1}$. The intermediate and deep layers of the Iceland

452 and Rockall basins were less ventilated, with AOU values higher than 45-50 µmol kg$^{-1}$. The
453 thermocline layer placed between 500 and 1000 m depth along these two basins presented the
454 highest maximum AOU throughout the period (>60 µmol kg$^{-1}$). The stagnation of these waters
455 corresponds with the high $C_T$ and low pH$_T$ (Figures 3a and 2d, respectively) encountered at
456 intermediate depths and should be considered in its temporal evolution.

457 The temporal distribution and trends of the average physicochemical properties (Figures 4, 5,
458 6, S4, S5 and S6) revealed remarkable heterogeneities in their interannual evolution within the
459 period 2009-2019 among the different basins and water masses. The interannual trends are
460 presented along with their respective standard error of estimate and correlation factors ($r^2$ and
461 p-value) in Table 2 and S4. The observed decrease in temperature and salinity, which was more
462 pronounced in subsurface layers, and its implication on the MCS variations were discussed in
463 section 4.

**4. Discussion**

**4.1.    Reversal of the physical trends during 2009-2019**

466 The present investigation revealed the cooling and freshening of the upper ocean in the
467 NASPG within the period 2009-2019 (Figure 4; Table 2), as recently reported since the reversal
468 of climatic trend and surface physical properties occurring after 2005 (Holliday et al., 2020;
469 Josey et al., 2018; Robson et al., 2016; Tesdal et al., 2018). The temperature decreased in the
470 upper ocean (with more than 95% level of confidence in SPMW, while non statistically
471 significant in ENACW) by 0.05-0.08 ºC yr$^{-1}$ (Table 2), which is consistent with the ratio of
472 heat loss per decade among the first 700 m depth equivalent to approximately -0.45 ºC decade$^{-1}$
473 $^{1}$ (-0.045 ºC yr$^{-1}$) encountered over the period 2005-2014 (Robson et al., 2016). The interannual
474 temperature trends in subsurface layers (Table 2) similarly draw the cooling observed in the
475 Irminger basin between 2008 and 2017 (-0.05 and -0.11 ºC yr$^{-1}$ for summer and winter,
476 respectively; Leseurre et al., 2020) and the winter average surface cooling along the entire
477 NASPG between 2004 and 2017 (-0.08 ± 0.02 ºC yr$^{-1}$; Fröb et al., 2019). The decrement in
478 subsurface salinity (with more than 95% level of confidence in both SPMW and ENACW) of
479 0.006-0.018 yr$^{-1}$ (Table 2) agreed with the interannual rates provided by Tesdal et al., (2018)
480 for the Irminger basin (-0.007 ± 0.002 yr$^{-1}$) and for the central-eastern NASPG (-0.020 ± 0.003
481 yr$^{-1}$) over the period 2004-2015.

482 The fluctuations in physical properties were linked to a decrease in oceanic heat transport and

483 storage within the NASPG, which has been attributed to changes in the AMOC over decadal

484 to multidecadal timescales (Balmaseda et al., 2007; Desbruyères et al., 2013; Mercier et al.,

485 2015; Smeed et al., 2018). However, the assessment of the temporal evolution of the AMOC

486 in high latitudes remains uncertain, and there is no evidence of its impact on physical patterns

487 across the NASPG on an interannual scale (Jackson et al., 2022). The changes in the

488 atmospherics forcing also account for the variability of the upper ocean physical properties

489 and can have a cumulative effect over several years (Balmaseda et al., 2007; Böning et al.,

490 2006; Eden and Willebrand, 2001; Marsh et al., 2005).

491 The distribution of the water mass properties, the processes of vertical and horizontal mixing

492 and the circulation patterns in the Irminger and Iceland basins were described by García-Ibáñez

493 et al., 2016 and 2018. The poleward path of the ENACW (Pollard et al., 1996) and its mixing

494 with waters moving from the west across the NASPG (Ellett et al., 1986) accounted for the

495 highest subsurface temperature and salinity signals observed in the Iceland basin and even

496 more in the Rockall Trough. The SPMW and LSW in the Rockall Trough exhibited higher

497 temperature and salinity signals in the respectively order of ~1ºC and ~0.05-0.1 compared to

498 the Irminger and Iceland basins (Figure 4). The NASPG circulation patterns account for these

499 differences by transporting eastward these water masses, which subduct below the ENACW

500 in the Rockall Trough and mixed with warmer and more saline intermediate waters (i.e.

501 Mediterranean Water) moving from the south (e. g. Ellett et al., 1986; Harvey, 1982; Holliday

502 et al., 2000).

503 The low temperature and salinity signals in the less-stratified Irminger basin (Figure 2)

504 experienced weaker interannual decreases in subsurface layers and higher rates of cooling and

505 freshening in intermediate and deep waters compared with the Iceland and Rockall basins

506 (Figure 4; Table 2). These longitudinal thermohaline heterogeneities were related to the

507 enhancement of vertical mixing processes in areas of water mass formation along the western

508 NASPG (Fröb et al., 2016; García-Ibáñez et al., 2015; Pickart et al., 2003; Piron et al., 2017)

509 and the water mass transformation along the NAC (Brambilla and Talley, 2008). The strongest

510 decrement in subsurface temperature and salinity along the Iceland and Rockall basins (Figure

511 4; Table 2) coincided with the significant event of heat loss and freshening observed by

Holliday et al., (2020) in the eastern NASPG over the period 2012-2016, so-called the Great Salinity Anomaly. This pattern was not easily discernible in the Irminger basin due to the transport of freshwater through the Fram Strait, as well as due the redirection of the Labrador Current combined with changing wind stress curl (Holliday et al., 2020).

**4.2.  Evaluation of the interannual trends in $C_T$ in response to changes in $C_{ant}$ and $C_{nat}$**

The changes in the physical patterns influenced the interannual variability of the MCS. The increase in $C_T$ expected in the upper ocean due to the atmospheric $CO_2$ uptake was offset by the cooling and freshening (and dealkalinization) of the subsurface layers. The observed rates of increase in $C_T$ (Table 2) did not show notable differences with respect to the interannual trends determined from previous decades at the Irminger and Iceland basins (0.62-0.82 and 0.38-0.64 µmol kg$^{-1}$ yr$^{-1}$, respectively; García-Ibáñez et al., 2016) and at IRM-TS and IS-TS (0.49-0.71 and 0.39-0.94 µmol kg$^{-1}$ yr$^{-1}$, respectively; Pérez et al., 2021). The interannual rates of increase in $NC_T$ were higher than those of $C_T$ in the subsurface layers, while the trends were similar among intermediate and deep layers (Table 2). A detailed description of the interannual $A_T$ trends is provided in Appendix B.

The entrance of $C_{ant}$ through the air-sea interface and its accumulation dominated the observed increase in $C_T$ (Figure 5 and Table 2). The increase in ventilation over 2009-2019, shown by the negative AOU trends (Figure S6 and Table S4), favoured the vertical mixing. The upper waters, due to be in contact with the atmosphere and have high biological production rates during the warm months, show high $C_{ant}$ and low $C_{nat}$ contents. The enhanced transport of upper waters toward the interior ocean explained the rapid growth in $C_{ant}$ at intermediate and deep layers. The $C_{ant}$ trends ranged between 0.85 and 1.77 µmol kg$^{-1}$ yr$^{-1}$ (statistically significant at the 99% level). They were higher than the observed on a decadal to multidecadal scale since the late 20th century in the Irminger and Iceland basins (0.21-0.89 µmol kg$^{-1}$ yr$^{-1}$ during 1991-2015,García-Ibáñez et al., 2016; and 0.38-1.15 µmol kg$^{-1}$ yr$^{-1}$ during 1983-2013, Pérez et al., 2021), which show the enhancement in the $C_{ant}$ accumulation on interannual scales during periods of high ventilation, as previously reported by Perez et al., (2008). The $C_{nat}$ show an inverse relationship with $C_{ant}$ at intermediate and deep layers ($r^2>0.5$; statistically significant at the 95% level of confidence) and weakly decreased across the western deep-convection

542 NASPG (Figure 5 and Table 2). The growth in phytoplankton biomass (Ostle et al., 2022),

543 together with the enhanced export toward the interior ocean under increasing ventilation,

544 account to the observed decrease in $C_{nat}$ in upper waters. The $C_{nat}$ showed a weaker decrease

545 at intermediate and deep layers due to the dominance of remineralization, which was not

546 intense enough at this time of the year to neutralize the downward transport of low-$C_{nat}$ water

547 from the surface but accounted to partially compensate for its effect. The observed variations

548 in $C_{nat}$ between years were strongly linked with fluctuations in the biological processes

549 explained its non-significant trends at several layers. The changes in the circulation pattern of

550 the NASGP and thus in the horizontal advection related with the climatological forcing

551 (Balmaseda et al., 2007; Desbruyères et al., 2013; Mercier et al., 2015; Thomas et al., 2008;

552 Xu et al., 2013) could behave as a source of variability for both $C_{ant}$ and $C_{nat}$ and also infers

553 differences between consecutive years.

554 The vertical distribution of $C_{ant}$ and $C_{nat}$ along the transect (Figure 3b and 3c) reflect the higher

555 stratification in the Iceland and Rockall basin compared to the well vertically-mixed Irminger

556 basin. It represents a source of variability in the interannual changes of $C_{ant}$ among the different

557 layers and basins (Figure 4; Table 2). In the western NASPG, the surface heat loss and

558 enhanced deep convection processes favour the solubility and subsequent uptake of

559 atmospheric $CO_2$ and inject oxygenated and $CO_2$-rich waters into deeper layers (Messias et al.,

560 2008). Its likely accounts for intermediate and deep layers in the Irminger basin exhibiting the

561 highest $C_{ant}$ accumulation rates in the NASPG (Figure 5; Table 2). The highest ventilation of

562 the interior ocean in the Irminger basin was demonstrated by its minimum AOU values (Figure

563 2 and S6). It induced a rapid surface-to-bottom transport of $C_{ant}$ shown by its highest rates of

564 increase in intermediate and deep waters throughout the region (Figure 5; Table 2). The high

565 $C_{ant}$ values and its rapidly increment at DSOW were explained by the improved oxygenation

566 of this layer at shallower depths (interannual AOU trends given in Table S4) and its subduction

567 through the continental slope below ISOW.

568 In the eastern NASPG, the stratification weakened due to the path of the NAC warming

569 eastward the upper water column and accounted to slowdown the increase in $C_{ant}$ in the Iceland

570 basin. An exception comes with the Rockall basin, in which the relatively warm and salty

571 ENACW (Figure 2 and 4) showed the maximum $C_{ant}$ (58-68 µmol kg$^{-1}$) and minimum $C_T$

572    (2120-2131 µmol kg$^{-1}$) and $C_{nat}$ (2058-2070 µmol kg$^{-1}$) throughout the region (Figure 3 and

573    5). The enhanced oxygenation of the ENACW (AOU <20 µmol kg$^{-1}$ and reaching the oxygen

574    saturation after 2014) was related with its high rates of renovation due to its path from the

575    south (Pollard et al., 1996) and its mixing with waters moving eastward (Ellett et al., 1986).

576    This favoured the transport subsurface waters with relatively high $C_{ant}$ content from lower

577    latitudes into the Rockall Trough and introduced wide differences respect to adjacent deeper

578    layers moved from the western NASPG which strength the stratification. As the NAC

579    transports nutrient-rich waters northward and eastward into subsurface layers in the Rockall

580    Trough, biological production tends to increase and actively reduced the $CO_2$ excess from the

581    ENACW (McGrath et al., 2012b), as proved by the observed low $C_T$ and $C_{nat}$. The ENACW

582    presented relatively low $C_{nat}$ and $C_T$ (Figure 5) and high $A_T$ and $NA_T$ in 2014. These variations

583    indicated that the increase in carbonate and bicarbonate concentrations rising $A_T$ and $NA_T$ was

584    compensated by the depletion in dissolved $CO_2$. The relatively high temperature and $NA_T$ in

585    2014 likely indicated an improved spreading of subsurface waters from subtropical latitudes

586    into the Rockall Trough. The enhanced biological production in these waters, together with the

587    reduction in solubility due to warming which favour the $CO_2$ evasion to the atmosphere,

588    account for decreasing $C_{nat}$ and thus $C_T$.

589    The strong interannual increase in the ENACW ventilation during this decade increase the $C_{ant}$

590    and decrease the $C_{nat}$ (Rodgers et al., 2009) keeping approximately constant the $C_T$ (Table 2).

591    The poorly ventilated thermocline (AOU > 60 µmol kg$^{-1}$), placed between 500-1000 m in the

592    eastern NASPG, induced a $C_{nat}$-driven increase in $C_T$ among the SPMW and uLSW. However,

593    its intrusion does not present relevant variations with time and thus does not introduce

594    differences in the interannual trends of the biogeochemical properties.

595    **4.3.    Acidification trends**

596    The interannual $pH_T$ trends (Figure 6, Table 2) exhibited the acidification of the whole water

597    column in NASPG during the period 2009-2019. Despite the acidification rates observed in

598    the most subsurface waters among the three basins were not significant at the 90% confidence

599    level (Table 2), they were consistent in the interval of 0.001 units yr$^{-1}$ to those observed during

600    larger periods at time-series stations located across the North Atlantic: at subtropical latitudes

601    ($0.0018 \pm 0.0002$ units yr$^{-1}$ during 1995-2014 and $0.0020 \pm 0.0001$ units yr$^{-1}$ during 1995-2023

602  at ESTOC, González-Dávila and Santana-Casiano, 2023; and $0.0017 \pm 0.0001$ units $yr^{-1}$ during

603  1983-2014 at BATS, Bates et al., 2014) and subpolar latitudes ($-0.0017 \pm 0.0002$ units $yr^{-1}$ at

604  IRM-TS during 1983-2013 and $-0.0026 \pm 0.0002$ units $yr^{-1}$ at IS-TS during 1985-2013,

605  summarized by Pérez et al., 2021). In addition, the changes in the surface $pH_T$ trends has been

606  reported by Leseurre et al., (2020) in the western NASPG within a wide latitudinal area (54-

607  64ºN) during the period 2008-2017 in comparison with the periods 1993-1997 and 2001-2007.

608  Although the highly significant cooling observed in SPMW, the year-to-year variations in

609  ventilation (shown by the annual average AOU and its trends in Figure S6) and thus in $C_{nat}$ and

610  $C_{ant}$ (Figure 5) introduced relevant changes in $pH_T$ on an interannual scale and explained the

611  low significant trends. The extreme negative NAO index of 2009-2010 (Jung et al., 2011)

612  weakened the wind forcing, which infers variability in the circulation patterns and physical

613  properties of the surface waters, consequently reducing deep convection. This was observed

614  in the slowdown in ventilation from 2009 to 2010 (Figure S6) in the Irminger and Iceland

615  basins which caused a relatively increase in $C_{nat}$ and decrease in $C_{ant}$ (Figure 5).

616  The highest acidification rates were found through intermediate and deep waters in the

617  Irminger and Iceland basins, coinciding with the highest rates of increase in $C_{ant}$ (Table 2,

618  trends statistically significant at more than 95% level of confidence). The exception comes

619  with the DSOW, which presented and interannual decrease in $pH_T$ in phase with those of the

620  uLSW. This singularity was previously observed by García-Ibáñez et al., (2016), which noticed

621  the similar trends between the DSOW and LSW attributed to the recently formation and sink

622  through the continental slope of the DSOW. The acidification rates found among the uLSW,

623  LSW and ISOW (0.0026-0.0032 units $yr^{-1}$) experienced, on an interannual scale, an

624  acceleration in comparison with previous reported based on long-term records [e. g. 0.0009-

625  0.0017 units $yr^{-1}$ estimated for 1981-2008 by Vázquez-Rodríguez et al., (2012b); 0.0013-

626  0.0016 units $yr^{-1}$ estimated for 1991-2015 by García-Ibáñez et al., (2016); 0.0015-0.0019 units

627  $yr^{-1}$ estimated for 1983-2013 at the IRM-TS by Pérez et al., (2021); $0.0019 \pm 0.0001$ units yr-

628  1 estimated for 1993-2017 by Leseurre et al., (2020)]. Contrasting the rates of change in $pH_T$

629  during the decade of study with those encountered by these multidecadal evaluations (and

630  considering the total amount of years comprising each of the studies and the changes in the ion

631  hydrogen concentration- $[H_T^+]$), we estimate an acceleration in the rates of acidification of 0.4-

632  5.4% in the Irminger basin and 1.0-9.0% in the Iceland basin during the 2010s since the late

633     20th century. This acceleration was mainly attributed to increased deep-water ventilation

634     (shown in the rapid decrease in AOU in Figure S6) favouring the progressively increase in the

635     accumulation of $C_{ant}$ and $C_{nat}$ toward intermediate a deep layers, in which cooling was not

636     significant in the Irminger basin and neither enough intense in both basins to compensate the

637     acidification.

638     Although the similarities encountered in the $pH_T$ trends among both basins, the average values

639     presented differences which may be closely linked with the transport and transformations of

640     the water masses along the NASPG and mainly modulated by the Reykjanes Ridge (García-

641     Ibáñez et al., 2015, 2016, 2018). The transformation of the SPMW formed in the Iceland

642     (McCartney and Talley, 1982; Brambilla and Talley, 2008; Tsuchiya et al., 1992; Van Aken and

643     Becker, 1996) and flowing with the NAC across the Reykjanes Ridge (Brambilla and Talley,

644     2008) accounted for the lower $pH_T$ values in the Irminger basin. The differences in $pH_T$ found

645     at intermediate and deep layers were related with the divergence of the LSW path into two

646     cores when it reaches the Reykjanes Ridge (Álvarez et al., 2004; Pickart et al., 2003) and the

647     ISOW path flowing southward along the western Iceland basin and recirculated northward into

648     the eastern Irminger basin (Dickson and Brown, 1994; Saunders, 2001). These differences in

649     the spreading of water masses enhanced the ventilation in the Irminger basin favouring the fall

650     in $pH_T$ compared with the Iceland basin. The rise in the ISOW following the Reykjanes Ridge

651     slope through its eastern flank favoured a strong vertical mixing over and around the ridge

652     (Ferron et al., 2014) and a reduction of the LSW core in the Iceland basin (García-Ibáñez et

653     al., 2015), contributing to resemble $pH_T$ values and trends among the uLSW and LSW in this

654     basin.

655     The upper waters of the Rockall Trough presented the maximum $pH_T$ throughout the transect

656     (8.02-8.08 units). The observed strong $pH_T$ fluctuations between years related with interannual

657     changes in the NAC do not allow to discern trends with a statistically interval of confidence

658     equal or higher than the 90%. The interannual decrease in $pH_T$ in the ENACW (~0.001 units

659     yr$^{-1}$) was half than the observed along southernmost transects in the Rockall Trough between

660     1991 and 2010 (~0.002 units yr$^{-1}$, McGrath et al., 2012a). The temporal distribution of the

661     average $pH_T$ (Figure 6) highly influenced by the high-ventilation (seen in minimum AOU

662     values highly variables between years and which tend to decrease with 99% statistical

663    confidence; Figure S6 and Table S4) allow to discern two periods: the approximately constant

664    ventilation rates keep a steady state in terms of $pH_T$ during 2009-2011, while the progressively

665    renewal and oxygenation of subsurface waters after 2012 (and peaking in this year) increase

666    the $pH_T$. The renewal of waters in the shallow Rockall Trough, in contrast with the

667    westernmost NASPG, was not primarily driven by vertical but by lateral advection. The

668    modifications of the ENACW through air-sea exchange and mixing with adjacent waters

669    modulated its properties at different time scales (Holliday et al., 2000) and caused the observed

670    variations in the MCS. The variations in $pH_T$ between consecutive years after 2012 may be

671    attributed to the fluctuations in the spreading into the Rockall Trough of several water masses

672    occupying different depths coming from the south and east (Ellett et al., 1986; Pollard et al.,

673    1996). Holliday et al., 2020 reported the reduction in the spreading of saline subsurface waters

674    from subtropical latitudes and diversion of Arctic freshwater from the western boundary into

675    the eastern NASPG during 2012-2016. The subsequent freshening of the ENACW

676    compensated for the increase in AT expected without the effect of salinity (see in the decreasing

677    AT against the increasing NAT; Figure S4 and Table S4) and weakened the increase in CT

678    expected due to poleward advection (see in the slowdown in the rise of CT in comparison with

679    those of NCT; Figure 5 and S5 and Table 2 and S4). The $C_T$ remains approximately constant

680    (Figure 5 and Table 2) due to the increase in $C_{ant}$ ($0.85 \pm 0.11$ µmol kg$^{-1}$ yr$^{-1}$; p-value < 0.01)

681    was neutralized by the decrease in $C_{nat}$ (-$0.84 \pm 0.50$ µmol kg$^{-1}$ yr$^{-1}$; p-value < 0.1). These

682    findings suggest that the atmospheric $CO_2$ invasion was offset by the growing phytoplankton

683    biomass favouring its biological uptake (Ostle et al., 2022) and the weakening transport of

684    remineralized and saline water from the south (Holliday et al., 2020), thus compensating the

685    acidification of the ENACW.

686    The SPMW among the Iceland and Rockall basins showed similar $pH_T$ trends (Table 2) due to

687    the emplacement of the poorly-oxygenated thermocline at these depths (García-Ibáñez et al.,

688    2016). The approximately constant AOU at SPMW in the eastern NASPG (Figure S6) proved

689    its steady ventilation, which can introduce differences in the acidification rates among the

690    layers accomplishing the Rockall Trough. The influence of the cooling and freshening of

691    deeper areas due to the spreading and horizontal mixing was notable in the LSW, which

692    presented slightly higher $pH_T$ values in the Rockall respect to the adjacent Iceland basin.

## 4.4. Interannual changes in $\Omega_{Ca}$ and $\Omega_{Arag}$

The analysis of the changes in $\Omega_{Ca}$ and $\Omega_{Arag}$ hold significance in elucidating the potential effects of OA over the $CaCO_3$ species calcite and aragonite, thereby offering insights into their potential implications for marine calcifying organisms and ecosystems. The vertical distribution of $\Omega_{Ca}$ and $\Omega_{Arag}$ is presented in Figure S3. The upper and intermediate layers up to 2100-2400 m depth of the Irminger and Iceland and the whole Rockall basin were supersaturated for aragonite ($\Omega_{Arag} > 1$), while the DSOW was undersaturated ($\Omega_{Arag} < 1$). The ISOW, with $\Omega_{Arag}$ ranged between 1.0 and 1.1 at the beginning of the decade, crossed to undersaturated conditions at the end of the period due to the progressively rise of the aragonite saturation horizon (depth in which $\Omega_{Arag} = 1$). The whole water column throughout the section was supersaturated for calcite ($\Omega_{Ca} > 1$) due to its lower solubility (Mucci, 1983). The $\Omega_{Ca}$ and $\Omega_{Arag}$ in the SPMW (2.2-2.7 and 1.4-1.7 units, respectively) were lower than the encountered equatorward in the subsurface Atlantic (>4.0 and >2.5 units, respectively; González-Dávila et al., 2010; González-Dávila and Santana-Casiano, 2023). The poleward pathway of low-latitude upper waters through the Rockall Trough explained the higher $\Omega_{Ca}$ and $\Omega_{Arag}$ found in the ENACW (3.0-3.6 and 1.8-2.3 units, respectively). The reduction in $\Omega_{Ca}$ and $\Omega_{Arag}$ towards higher latitudes in upper and intermediate layers smooth the vertical gradients in the NASPG compared with the subtropical latitudes (González-Dávila et al., 2010; González-Dávila and Santana-Casiano, 2023).

The correlation of $\Omega$ with $pH_T$ ($r^2 = 0.90$) with a level of significance higher than the 99% explained that the individual components driving OA accompanied the declining in $\Omega$. The interannual trends in $\Omega_{Ca}$ and $\Omega_{Arag}$ (Figure 7, Table 2) exhibited the decrement through the whole water column along the NASPG with a level of statistical confidence generally higher than the 90%. The rates of declining for $\Omega_{Ca}$ and $\Omega_{Arag}$ in the SPMW (0.011-0.021 and 0.007-0.013 units yr-1; respectively) were consistent with the trends observed up to 100 m depth at ESTOC between 1995 and 2023 ($0.019 \pm 0.001$ and $0.012 \pm 0.001$ units yr$^{-1}$, respectively; González-Dávila and Santana-Casiano, 2023) and in surface waters at the IS-TS between 1985 and 2008 ($0.0117 \pm 0.0011$ and $0.0072 \pm 0.0007$ units yr$^{-1}$, respectively; Olafsson et al., 2009). The $\Omega_{Arag}$ trend estimated for SPMW in the Irminger basin ($-0.007 \pm 0.003$ units yr$^{-1}$) is consistent with that reported for surface waters by Bates et al., (2014) over 1983-2014 (-0.008

723    ± 0.004 units yr$^{-1}$) and fall within the range of those estimated during summer by Leseurre et

724    al., 2020 over 2008-2017 (-0.005 ± 0.001 units yr$^{-1}$). Chau et al., 2014 recently deduced from

725    reconstructed products a slower decrease (-0.004 ± 0.001 units yr$^{-1}$), highlighting the large

726    uncertainty in the estimations of interannual trends for pH and $\Omega_{Arag}$ across the NASPG due to

727    the low-data sampling frequency at their monitoring sites. The declining in $\Omega_{Arag}$ in the SPMW

728    accelerated by ~26% and ~51% in the Irminger and Iceland basins, respectively, in comparison

729    with the trends given for the period 1991-2018 (0.0052 ± 0.0006 and 0.0049 ± 0.0015 units yr$^{-}$

730    $^{1}$, respectively; García-Ibáñez et al., 2021). The observed decrease in $\Omega_{Arag}$ in the SPMW was

731    ~23% faster in the Rockall Trough than in the adjacent Iceland basin. The interannual declining

732    for $\Omega_{Ca}$ and $\Omega_{Arag}$ in the ENACW (0.012 and 0.008 units yr$^{-1}$, respectively) agreed with these

733    previous observations but were not statistically significances likely due to the high variability

734    modifying the changes in pH$_T$ in this layer (see section 4.2). Despite the acceleration of the

735    acidification rates toward intermediate and deep layers, the declining rates weakened for $\Omega_{Ca}$

736    and even more for $\Omega_{Arag}$ (Table 2). Moreover, the vertical profiles were approximately constant

737    throughout the section in contrast with the heterogeneous vertical distribution of pH$_T$ between

738    basins. This behaviour was previously observed in the Irminger and Iceland basins by García-

739    Ibáñez et al., (2021) and explained by pressure and temperature-induced changes in the

740    speciation of the $CO_2$-carbonate chemistry species (Jiang et al., 2015) and in the solubility of

741    calcite and aragonite (Mucci, 1983). Their combined action counterbalanced the alterations in

742    $\Omega$ resulting from acidification, particularly in colder deep waters where the solubility of calcite

743    and aragonite was reduced (García-Ibáñez et al., 2021). However, the fall down in $\Omega_{Ca}$ and

744    $\Omega_{Arag}$ along the uLSW, LSW and ISOW accelerated by 40-75% in relation with the trends

745    reported by García-Ibáñez et al., (2021) for the Irminger and Iceland basins. The LSW and

746    ISOW presented faster declining rates for $\Omega_{Ca}$ and $\Omega_{Arag}$ in the Irminger (Table 2), which may

747    be caused by the enhanced ventilation of the interior ocean which accelerated the acidification

748    (see section 4.2). The westward rise in depth of these layers along the Greenland continental

749    slope, accompanied by a subsequent elevation in the horizons of solubility, resulted in reduced

750    buffering capacity against acidification effects in the Irminger basin when compared to the

751    Iceland basin. In contrast, the rise in depth of LSW in the Rockall Trough favour the increment

752    of ~0.2 units in $\Omega_{Ca}$ and $\Omega$Arag with respect to the Iceland basin but had not influence on the

753    interannual trends, which were coinciding. The $\Omega_{Ca}$ and $\Omega_{Arag}$ in the DSOW, despite showed a

trend accelerated by ~30% compared to the observed by García-Ibáñez et al., (2021), presented the weakest interannual decreases throughout the section ($0.004 \pm 0.003$ and $0.002 \pm 0.001$ units yr$^{-1}$, respectively) due to the high pressure and low temperatures compensating the rapidly acidification (Figure 6, Table 2).

The decrease in $\Omega$ could have severe consequences on organisms reliant on aragonite, which is less resistant to dissolution than calcite (Mucci, 1983; Broecker and Peng, 1983) and thus expected to experience relatively higher susceptibility to the effects of OA over shorter time scales (Raven et al., 2005). The progressive reduction in $\Omega_{Arag}$ is driving a long-term decrease in the depth of the aragonite saturation horizon ($\Omega_{Arag}=1$) by 80-400 m since the preindustrial era (Álvarez et al., 2003; Feely et al., 2004; Pérez et al.,2013, 2018; Pérez et al., 2013; Tanhua et al., 2007; Wallace, 2001) and is projected to shoal by more than 2000 m by the end of the century under the IS92a scenario (Orr et al., 2005). The vertical section of $\Omega_{Arag}$ in Figure S3 shows the shallower aragonite saturation horizon during 2009 and 2016 compared to preindustrial times. Likewise, Orr et al., (2005) suggested that high-latitudes surface waters could become undersaturated when the atmospheric $CO_2$ concentration double the preindustrial concentration within the next 50 years. It would reduce the calcification rates in some shallow calcifying organism by more than the 50% (Feely et al., 2004).

The planktonic aragonite-producers pteropods (e. g. *Limacina helicina, Clio pyramidata*), which have high population densities in subpolar regions up 300 m depth (Bathmann et al., 1991; Urban-Rich et al., 2001) and play a key role in the export flux of both carbonate and organic carbon (Accornero et al., 2003; Collier et al., 2000), are expected to be highly vulnerable to OA if the aragonite saturation horizon continue to shoal (Orr et al., 2005). The undersaturation toward intermediate and upper layers negatively influence the aragonite-based CWC (e. g. *Lophelia pertusa, Madrepora oculate*), which show their highest diversity and population along the NASPG between 200 and 1000 m depth among the global ocean (Roberts et al., 2009). In fact, several studies reported that CWC ecosystems are anticipated to be among the first deep-sea ecosystems to experience acidification threats (Gehlen et al 2014; Guinotte et al., 2006; Maier et al., 2009; Raven et al., 2005; Roberts et al., 2009; Turley et al., 2007), particularly in the North Atlantic (Perez et al., 2018). The findings presented here contribute to a deeper understanding of the biological impacts of OA along the NASPG.

## 4.5. Processes controlling OA and $\Omega$ trends

Due to the variety of processes involved in OA, a decomposition of the $pH_T$ and $\Omega$ trends into the individual components that govern their spatio-temporal variability was done (see section 2.2.6). The interannual variations in $pH_T$ ($\frac{dpH_T}{dt}$) and $\Omega$ ($\frac{d'\Omega}{dt}$) explained by fluctuations in temperature ($\frac{\partial pH_T}{\partial T}\frac{\partial T}{dt}$ and $\frac{\partial'\Omega}{\partial T}\frac{\partial T}{dt}$) , salinity ($\frac{\partial pH_T}{\partial S}\frac{\partial S}{dt}$ and $\frac{\partial'\Omega}{\partial S}\frac{\partial S}{dt}$), $A_T$ ($\frac{\partial pH_T}{\partial A_T}\frac{\partial A_T}{dt}$ and $\frac{\partial'\Omega}{\partial A_T}\frac{\partial A_T}{dt}$) and $C_T$ ($\frac{\partial pH_T}{\partial C_T}\frac{\partial C_T}{dt}$ and $\frac{\partial'\Omega}{\partial C_T}\frac{\partial C_T}{dt}$) were calculated for each layer and basin (Eq. 2) and summarized in Table 3 and 4. The positive contributions of each of the drivers indicate increments while negative contributions the opposite. The cumulative changes resulting from the distinct drivers (referred to with the subscript "calculated" in Table 3 and 4) were consistent with the observed $pH_T$ trends (referred to with the subscript "obs" in Table 3 and 4), thereby instilling confidence in the methodology. An exception was found at the DSOW, in which the strong $NA_T$ decrease had a crucial influence on declining $\Omega$.

The minimal differences between observed and calculated rates of change have added coherence to the non-significant trends identified for $pH_T$ and $\Omega$ trends and/or its drivers in some basins and layers (Table 2, 3 and S4). In the entire section at SPMW, the $\frac{dpH_T}{dt}$ (calculated), explained by the cumulative impact of its drivers (all of them statistically significant at the 95% level of confidence), aligns within a range of <0.0002 units yr$^{-1}$ with $\frac{dpH_T}{dt}$ (obs) (which was not significant). In the Irminger and Iceland basins at intermediate and deep layers, the $\frac{dpH_T}{dt}$ (obs) (statistically significant at least at the 95% level of confidence) were consistent within the range of <0.001 units yr$^{-1}$ with $\frac{dpH_T}{dt}$ (calculated) (T, S and NA$_T$ shows non-significant trends at some of the intermediate and deep layers). The interannual variations were non-significant for $pH_T$ neither for its drivers in the Rockall Trough at LSW and ENACW. The high temporal dispersion of average data in these layers was mainly related to the rise in depth of LSW along the eastern continental slope and its mixing with shallower waters coming from subtropical latitudes (Ellett et al., 1986; Harvey, 1982; Holliday et al., 2000). The substantial variability in the Rockall Trough made it difficult to discern OA patterns and its drivers on an interannual scale. Therefore, long-term monitoring and the development of multidecadal-scale studies are required in this area to derive significant conclusions.

812  The cooling and freshening modified the physical-driven $pH_T$ changes compared with those

813  encountered by García-Ibáñez et al., (2016) during previous decades in the western NASPG.

814  The cooling contributed to increase the $pH_T$ and compensated the observed acidification rate.

815  The increase in $pH_T$ due to temperature fluctuations was maximum at SPMW (~0.001 units yr$^{-1}$

816  ) and negligible in deeper layers (<0.0003 units yr$^{-1}$ at uLSW and below). The increase in $pH_T$

817  due to salinity fluctuations was minimal (<0.0001 units yr$^{-1}$) through the whole water column

818  in the three basins, reflecting that the observed freshening caused insignificant changes in $pH_T$.

819  The temperature and salinity contributed by 19.1-26.5% and 1.2-3.3%, respectively, in the total

820  $pH_T$ change in the upper layers, while presented an influence three times lower toward the

821  interior ocean (1.3-7.6% and <0.6%, respectively). The enhanced convective processes in the

822  Irminger basin (e. g. Fröb et al., 2016; García-Ibáñez et al., 2015; Gladyshev et al., 2016a,

823  2016b; Piron et al., 2017) together with the rapid transport of LSW from the Labrador Sea to

824  the Irminger basin (Yashayaev et al., 2007) introduced differences in the thermal-driven $pH_T$

825  with the Iceland basin, as previously reported by García-Ibáñez et al., (2016). The advection

826  of LSW through the Greenland continental slope also affected the DSOW (Read, 2000;

827  Yashayaev and Dickson, 2008), which shows thermal-driven $pH_T$ changes consistent with

828  those encountered through the LSW in the Irminger basin.

829  Despite the negligible direct contribution of the salinity fluctuations over the $pH_T$ changes, the

830  freshwaters fluxes influence the distribution of $A_T$ and $C_T$ indirectly affecting $pH_T$ trends. After

831  removing salinity effects, $NA_T$ show positive trends in subsurface layers and negative trends

832  toward the interior ocean (Figure S4 and Table S4; detailed in Appendix B). The changes in

833  $NA_T$ described the 7.8-10.1% of the total $pH_T$ change at SPMW. The $NA_T$-driven $pH_T$ changes

834  weakened with depth (Table 3) due to the insignificantly interannual changes in $NA_T$ through

835  LSW and ISOW (Table S4). The weak contribution of $NA_T$ in these layers (1.3-5.1%) could be

836  related to the difficulty of reversing the large alkalinization until the 2000s resulted from the

837  slowdown in the formation of LSW since the mid-90s (Lazier et al., 2002; Yashayaev, 2007),

838  which was transmitted towards deeper overflow waters (Sarafanov et al., 2010). The

839  substantial interannual changes and the abrupt change between periods of increase and

840  decrease of the seawater properties at DSOW (Yashayaev et al., 2003; Stramma et al., 2004)

841  linked with changes in the LSW formation (Dickson et al., 2002) explained the rapidly

842  decrease in $NA_T$ (Table S4), which described the 14.6% of the $pH_T$ declining.

843   The increase in $NC_T$ drove by the rise in $C_{ant}$ was found to govern the acidification, with a

844   contribution higher than the 67% across the entire water column. The $NC_T$-driven $pH_T$

845   declining was close to twice the observed and calculated acidification rates through the SPMW

846   (Table 3). However, the contribution of $NC_T$ at SPMW (67-69%) was lower than the

847   encountered toward the interior ocean (82-96%) due to the relevance of temperature and $A_T$

848   over $pH_T$ trends in the upper layers. The cooling and increase in $NA_T$ counteracted the

849   acidification expected by the increasing $C_T$ at SPMW by 28-34% and 11-15%, respectively. In

850   intermediate and deep layers, the thermal-neutralization of the $C_T$-driven acidification was

851   weaker (1.5-9.3%) and the decreasing $NA_T$ contributed to decrease the $pH_T$ by < 15%.

852   Freshening played a minor role in countering acidification (<6% in upper layers and <2% in

853   the interior ocean).

854   In line with declining $pH_T$, 79-83% of the decrease in $\Omega$ in subsurface layers was attributed to

855   the $C_{ant}$-driven rise in $NC_T$, with this influence reaching up to 97% in deeper waters. The

856   increase in $NA_T$ in the SPMW accounted by 10.4-13.0% in the $\Omega$ trends and counteracted its

857   $NC_T$-driven decrease by 12.6-16.2%. The contribution of $NA_T$ fall and reversed toward deeper

858   waters, explained <6% of the decline in $\Omega$ in the uLSW, LSW and ISOW in the Irminger basin

859   and <11% in the Iceland basin. The pronounced impact of the rapid decrease in $NA_T$ on the

860   acidification of the DSOW (see section 4.3) depicted the greater contribution of $NA_T$

861   encountered among the Irminger basin (16%) and compensated the $NC_T$-driven decrease in $\Omega$

862   by 36.4%. In the Rockall Trough, the contribution of $NC_T$ changes on $\Omega$ was reduced at LSW

863   (78.2-79.0%) compared to the Irminger basin (94.5%) while the effect of $NA_T$ fluctuations

864   tripled until reach 12.6-12.7%.

865   Despite the crucial role of cooling in mitigating acidification, temperature fluctuations have

866   an opposite effect on $\Omega$ due to the thermodynamic relationship inherent in the acid-base

867   equilibrium of the $CO_2$-carbonate system (Dickson and Millero, 1987). In the Irminger and

868   Iceland basins, the observed decrease in temperature contributed negligibly to the decline in

869   $\Omega$ (3.6% in the SPMW and less than 2% in intermediate and deep waters). The influence of

870   salinity, as with the $pH_T$ trends, was minimal: the observed freshening slightly elevated the

871   $\Omega$ trends, offsetting the decline by 4.6-4.7% in the SPMW, 1.1-2.1% in the uLSW and LSW,

872   and 0.5-1.2% in the ISOW and DSOW. Even with the slightly faster cooling and freshening

873    observed in the Rockall Trough, the contributions of temperature and salinity to $\Omega$ did not

874    exceed 7% in any of its layers.

## 5.  Conclusions

876    This research has evaluated the interannual changes in the basin-wide MCS dynamics along

877    the NASPG during 2009-2019. Despite the observational period is relatively short to quantify

878    long-term trends and to formulate significant future projections, the finding has allowed to

879    evaluate the ocean response, in terms of MCS dynamics and on an interannual scale, to changes

880    in deep-water convection and to isolate events affecting the physical patterns. The assessment

881    of OA within the Irminger and Iceland basins was enhanced by supplying novel data and trends

882    spanning a decade in which the physical patterns reversed. Additionally, the study provides an

883    unprecedent analysis of the physico-chemical variations in the Rockall Trough, which is

884    crucial for the assessment of the entire longitudinal span of the NASPG. It facilitates a more

885    accurate understanding of the mechanisms dictating basin-scale acidification processes and

886    advances our understanding of OA in the North Atlantic and Global Ocean.

887    Overall, the entrance and accumulation of $C_{ant}$ and interannual acidification trends were

888    strongly affected by the cooling, freshening and enhancement in the oxygenation during this

889    decade. The longitudinal span of the NASPG and the differences in circulation patterns, water

890    masses and bathymetry behaved as a source of spatio-temporal variability.  The interannual

891    acidification trends of the main water masses across the NASPG ranged between 0.0006-

892    0.0032 units yr-1 and caused a decline in the $\Omega$Ca and $\Omega$Arag of 0.004-0.021 and 0.003-0.013

893    units yr-1, respectively. The convective processes increased the accumulation rates of Cant in

894    the interior ocean by 50-86% and accelerated the acidification rates by around 10% compared

895    to previous decades in the Irminger and Iceland basins. The shallower hydrography of the

896    Rockall Trough and the poleward circulation patterns accounted for differences in the

897    acidification rates respect to surrounding waters.

898    The Cant-driven increase in NCT was found to govern the acidification of the NASPG with

899    contributions exceeding 60%. The combined effect of the decreasing temperature, salinity and

900    NAT neutralized close to one-half of the acidification along the entire longitudinal span of the

901    SPMW.  The enhanced deep-water ventilation in the western NASPG slowdown the cooling

and freshening toward the interior ocean, weakening the physical counterbalance of acidification.

The present investigation emphasizes the progressively increase in the uptake and accumulation of Cant and subsequent acceleration of OA along the NASPG. Novel data and results provided could be compared with other repeated hydrographic section data at mid and high latitudes in the North Atlantic, such as the A02, A25, AR07E and AR28 framed in the GO-SHIP program, as well as used in conjunction to develop future investigations. Additionally, they contribute to the improvement of the projections pertaining to the future state of the oceans run by models and forecast. Considering the important variability in the mechanism controlling the distribution of the physico-biogeochemical properties and particularly the OA in the North Atlantic, this research aims to highlight the necessity of continue monitoring and sampling the whole water column through repeated hydrographic sections, especially through the highly variable but less assess easternmost part.

**Appendix A: Correction of Dissolved Oxygen records for the cruise of 2019**

The sensor-measured DO data for the cruise of 2019 were corrected by considering the DO output data given by the neural network ESPER_NN (Carter et al., 2021) for the cruises of 2016 and 2019 (hereinafter ESPER-estimated DO) and the WINKLER-measured DO during the cruise of 2016. Among the 16 equations provided by the ESPER_NN that differently combines seawater properties as predictors, we use the equation 8 which only need as inputs the T and S (due to lack of measured macronutrients during the cruise of 2019) along with latitude, longitude, depth and date (see Table 2 in Carter et al., 2021). The reported Root Mean Squared Error (RMSE) of equation 8 for DO estimations in the global ocean is $\pm$ 9.7 µmol kg-1, which is reduced for intermediate waters (1000-1500 m) to $\pm$ 5.9 µmol kg$^{-1}$ (see Table 7 in Carter et al., 2021). Additionally, a new set of DO for 2019 based on WINKLER data for 2016 was computed, which was referred in this study as "pseudo-WINKLER" data. The difference between WINKLER-measured and ESPER-estimated DO during 2016 was interpolated to the longitudes and depths of the samples of 2019 by applying Delaunay Triangulation. The pseudo-WINKLER data was described as the sum of these interpolated differences and the ESPER-estimated DO data for 2019. The longitudinal distribution of measured and ESPER-

931   estimated DO data for 2016 and 2019 is depicted in Figure S1a and S1b. The interpolated

932   pseudo-WINKLER data for the cruise of 2019 were included in Figure S1a.

933   The sensor records of DO in 2019 were in average 4.90 µmol kg$^{-1}$ lower than the ESPER-

934   estimated and 10.31 µmol kg$^{-1}$ lower than the pseudo-WINKLER. A higher discrepancy was

935   observed in the average sensor-measured DO in the east part (237.60 ± 15.00 µmol kg$^{-1}$)

936   compared with the west part (281.40 ± 14.75 µmol kg$^{-1}$). The average differences (measured

937   minus ESPER-estimated DO and measured minus pseudo-WINKLER DO, $\Delta DO_{meas\text{-}ESPER}$ and

938   $\Delta DO_{meas\text{-}pseudoWINLKER}$, respectively; Figure S2c and S1d) shows that the sensor records were

939   strongly underestimated in the east part (-20.98 ± 10.91 and -28.77 ± 12.60 µmol kg$^{-1}$,

940   respectively) and weakly overestimated in the west part (8.59 ± 8.53 and 5.18 ± 12.02 µmol

941   kg$^{-1}$, respectively) during the cruise of 2019. These differences were corrected separately west

942   and east of 21.5ºW by using the relationship $\frac{\Delta DO_{meas-pseudoWINKLER}}{measured\ DO}$. The averages of this

943   relationship in the west and east part of the transect (0.016 and -0.12 µmol kg$^{-1}$, respectively)

944   were used as corrector factors. The corrected DO values were given by the product between

945   the measured DO and $\left(1 - \frac{\Delta DO_{meas-pseudoWINKLER}}{measured\ DO}\right)$.

**Appendix B: Interannual trends of $A_T$ and $NA_T$**

947   The interannual trends of $A_T$ (Figure S4 and Table S4) was found to be highly impacted by

948   freshening, with decreasing rates ranging from -0.33 to -0.71 µmol kg$^{-1}$ yr$^{-1}$ among the

949   SPMW and ENACW and from -0.01 to -0.18 µmol kg$^{-1}$ yr$^{-1}$ within the uLSW, LSW, ISOW

950   and DSOW. It contrasts with the minimal interannual changes and slight rates of increase in

951   $A_T$ encountered among the different layers by García-Ibáñez et al., (2016) from 1991 to 2015

952   in the Irminger basin (between 0.10 and 0.28 µmol kg$^{-1}$ yr$^{-1}$) and Iceland basin (between -

953   0.04 and 0.07 µmol kg$^{-1}$ yr$^{-1}$), and with the trends reported for the period 1983-2013 by Pérez

954   et al., (2021) at the IRM-TS (between 0.13 and 0.22 µmol kg$^{-1}$ yr$^{-1}$) and at the IS-TS (between

955   -0.04 and 0.15 µmol kg$^{-1}$ yr$^{-1}$). These heterogeneities in the temporal evolution of the $A_T$ were

956   driven by the decadal salinification of the whole water column observed since the late 20th

957   century and interrupted by interannual freshening episodes such as during the 2010s.

958   The interannual increase in $NA_T$ in upper layers could be related to acidification, which favour

959   the dissolution of carbonates, combined with increasing biological production reported for

960    upper layers across the NASPG (Ostle et al, 2022). It contrasts with the constant to weakly

961    decrease in $NA_T$ at intermediate and deep layers, in which the accelerated acidification was

962    compensated by the dominance of remineralization processes over lower biological uptake.

963    Consequently, the positive $NA_T$ trends encountered in the upper layers lead a rise in $pH_T$,

964    while the diminished $NA_T$ contributed to decrease the $pH_T$ toward the interior ocean.

965    The $A_T$/S relationship has increased at a rate of $0.5 \pm 0.2$ µmol kg$^{-1}$ yr$^{-1}$ (p-value < 0.05) due

966    to the combined action of the freshening (Figure 4) and the progressive increase of $A_T$-rich

967    water inflows through upper layers (observed in the positive trends of $NA_T$ in SPMW and

968    ENACW; Figure S4). This was likely associated with the stagnation of $A_T$-rich subtropical

969    waters in the upper layers due to the slowdown of the NASPG since the mid-90s (e.g., Böning

970    et al., 2006; Häkkinen and Rhines, 2004), along with changes in the spreading of waters from

971    higher latitudes influenced by melting.

972    **Code Availability**

973    MATLAB    and    R    codes    for    CANYON-B    are    available    at
974    https://github.com/HCBScienceProducts/CANYON-B. MATLAB and R code for ESPER_NN
975    are    available    at    https://github.com/BRCScienceProducts/ESPER.    MATLAB    code    for
976    anthropogenic    carbon    calculation    is    available    at
977    http://oceano.iim.csic.es/_media/cantphict0_toolbox_20190213.zip. The CO$_2$SYS programme
978    for MATLAB is available at https://github.com/jonathansharp/CO2-System-Extd.

979    **Data Availability Statement**

980    The measured surface-to-bottom CLIVAR data (2009-2019) used in this investigation are
981    published in open-access at Zenodo (DOI: 10.5281/zenodo.10276221). The GO-SHIP A25-
982    OVIDE    data    for    the    cruise    of    2018    is    available    at    SEANOE
983    (https://www.seanoe.org/data/00762/87394/).

984    **Author contribution**

985    DCH contributed with data analysis and wrote the manuscript. FFP, DCH, AV, DGS, AGG,
986    MGD and JMSC worked on the design, conceptualization and data preparation. SG, AS, MGD,
987    JMSC, AGG and DGS participated in 8, 4, 7, 7, 2 and 2 cruises, respectively. SG and AS were
988    the Chief Scientist in all cruises and responsible for the operational and maintenance
989    procedures for the CTD and additional sensors and thus for physical and sensor-measured
990    variables. MGD and JMSC got the funding acquisition and provision of resources for the
991    Spanish team from the ULPGC. SG and AS got the funding for ship time and provision of
992    resources for all the cruise participants. All authors critically revised the manuscript.

## Competing interest

The authors declare that the research was conducted in the absence of any commercial or financial relationships that could be construed as a potential conflict of interest.

## Acknowledgement

The participation on the cruises for the Spanish Team from the ULPGC was funded by the Science Spanish Ministry under the Complimentary Actions CTM2008-05255, CTM2010-09514-E and CTM2011-12984-E (years 2009-2011), the FP7 European project CARBOCHANGE under grant agreement no. 264879 and by the Spanish Innovation and Science Ministry through the Projects EACFe (CTM2014-52342-P) and ATOPFe (CTM2017-83476-P). SG and AS were supported by FMWE-2023-0002. FFP and AV were supported by the BOCATS2 (PID2019-104279GB-C21) project funded by MCIN/AEI/10.13039/501100011033 and by EuroGO-SHIP project (Horizon Europe #101094690). The participation of DCH was funded by the PhD grant PIFULPGC-2020-2 ARTHUM-2. Special thanks go to the technician and researchers Adrian Castro Álamo (2 cruises), Anna Barrera Galderique (3 cruises), Rayco Alvarado Medina (2 cruises) and Pilar Aparicio Rizzo (1 cruise) who helped with in situ analysis. We also thanks technicians at the P. P. Shirshov Institute of Oceanology from the Russian Academy of Science for the in situ analysis of dissolved oxygen and nutrients.

 **Legend for figures**

 Figure 1. (a) Map of the North Atlantic Subpolar Gyre (NASPG) with the schematic diagram
of the surface and deep circulation patterns compiled from Lherminier et al., (2010); Pérez et
al., (2021); Sarafanov et al., (2012); Schmitz and McCartney, (1993); Schott and Brandt,
(2007) and Sutherland and Pickart, (2008). The acronyms are defined as follow: the
bathymetric features are shown in grey (RR: Reykjanes Ridge, HB: Haton Bank, GBB: George
Bligh Bank, CGFZ: Charlie-Gibbs Fracture Zone, GIR: Greenland-Iceland Ridge, and GSR:
Greenland-Scotland Ridge), the surface currents are shown in orange (NAC: North Atlantic
Current, and IC: Irminger Current) and the deep water circulation is shown in blue and purple
(ISOW: Iceland-Scotland Overflow Water, DSOW: Denmark Strait Overflow Water, LSW:
Labrador Sea Water, and DWBC: Deep Western Boundary Current). The longitudinal
distribution of the surface-to-bottom sampling stations along the cruise track of 2016 (repeated
throughout the cruises) is shown with red dots. The black lines along the cruise track delimited
the three basins. (b) Vertical distribution of the water masses considered in this study for each
of the basins. The isopycnals, plotted over the salinity distribution for the cruise of 2016, show
the limits of the layers and were defined by potential density (in kg m$^{-3}$) referred to 0 dbar ($\sigma_0$).
The vertical gray lines show the limits between basins. The water masses (ENACW: Eastern
North Atlantic Central Water, SPMW: Subpolar Mode Water, uLSW: upper Labrador Sea
Water, LSW: Labrador Sea Water, ISOW: Iceland-Scotland Overflow Water, DSOW: Denmark
Strait Overflow Water) and the selection of potential density values delimiting the layers are
described in section 2.2.4. Figure produced with Ocean Data View (Schlitzer, 2021).

Figure 2. Water-column distribution along the longitudinal transect of (a) temperature, (b)
salinity, (c) $A_T$, (d) $pH_T$ and (e) AOU for the cruises of 2009 (left plots) and 2016 (right plots).
The vertical white lines show the limits between basins. Figure produced with Ocean Data
View (Schlitzer, 2021).

Figure 3. Water-column distribution along the longitudinal transect of (a) $C_T$, (b) $C_{ant}$ and (c)
$C_{nat}$ for the cruises of 2009 (left plots) and 2016 (right plots). The vertical white lines show the
limits between basins. Figure produced with Ocean Data View (Schlitzer, 2021).

Figure 4. Temporal distribution (2009-2019) of the average temperature and salinity in each of
the layers considered for the Irminger (left plot column), Iceland (central plot column) and
Rockall basins (right plot column). The average values were calculated for each cruise and
layer and represented with coloured points together with their respective error bars at the time
of each cruise (the method used for calculations was described in section 3.2). In the Irminger
plots, the empty points represent the average values for 2019 calculated with the measured
data available in the easternmost part of the basin (sampled part during this cruise), while the
coloured points for 2019 represent the average values corrected with A25-OVIDE-2018 data.
The interannual trends were given by linear regression of the average values, with the values
of the slope, the standard error of estimate and the $r^2$ presented in Table 2.

Figure 5. Temporal distribution (2009-2019) of the average $C_T$, $C_{ant}$ and $C_{nat}$ in each of the
layers considered for the Irminger (left plot column), Iceland (central plot column) and Rockall
basins (right plot column). The average values were calculated for each cruise and layer and
represented with coloured points together with their respective error bars at the time of each
cruise (the method used for calculations was described in section 3.2). In the Irminger plots,
the empty points represent the average values for 2019 calculated with the measured data

available in the easternmost part of the basin (sampled part during this cruise), while the coloured points for 2019 represent the average values corrected with A25-OVIDE-2018 data. The interannual trends were given by linear regression of the average values, with the values of the slope, the standard error of estimate and the $r^2$ presented in Table 2.

Figure 6. Temporal distribution (2009-2019) of the average $pH_T$ (in situ temperature) in each of the layers considered for the Irminger (left plot column), Iceland (central plot column) and Rockall basins (right plot column). The average values were calculated for each cruise and layer and represented with coloured points together with their respective error bars at the time of each cruise (the method used for calculations was described in section 3.2). In the Irminger plots, the empty points represent the average values for 2019 calculated with the measured data available in the easternmost part of the basin (sampled part during this cruise), while the coloured points for 2019 represent the average values corrected with A25-OVIDE-2018 data. The interannual trend were given by linear regression of the average values, with the values of the slope, the standard error of estimate and the $r^2$ presented in Table 2.

Figure 7. Temporal distribution (2009-2019) of the average $\Omega Ca$ and $\Omega Arag$ in each of the layers considered for the Irminger (left plot column), Iceland (central plot column) and Rockall basins (right plot column). The average values were calculated for each cruise and layer and represented with coloured points together with their respective error bars at the time of each cruise (the method used for calculations was described in section 3.2). In the Irminger plots, the empty points represent the average values for 2019 calculated with the measured data available in the easternmost part of the basin (sampled part during this cruise), while the coloured points for 2019 represent the average values corrected with A25-OVIDE-2018 data. The interannual trends were given by linear regression of the average values, with the values of the slope, the standard error of estimate and the $r^2$ presented in Table 2.

**Legend for Tables**

Table 1. Metadata list of hydrographic cruises.

Table 2. Interannual trends of temperature, salinity, $C_T$, $C_{ant}$, $C_{nat}$, $pH_T$, $\Omega Ca$ and $\Omega Arag$ in each of the layers and basins. The ratios of change were based on linear regressions applied to the average values (as represented in Figures 4-7) and presented together with its Standard error of estimate. The correlation coefficients $r^2$ and p-values were also provided. Values in bold denote trends statistically significant at the 95% level of confidence.

Table 3. Temporal changes in $pH_T$ (**in $10^{-3}$ units yr$^{-1}$**) explained by fluctuations in temperature $\left(\frac{\partial pH_T}{\partial T}\frac{\partial T}{dt}\right)$, salinity $\left(\frac{\partial pH_T}{\partial S}\frac{\partial S}{dt}\right)$, $A_T$ $\left(\frac{\partial pH_T}{\partial A_T}\frac{\partial NA_T}{dt}\right)$, and $C_T$ $\left(\frac{\partial pH_T}{\partial C_T}\frac{\partial NC_T}{dt}\right)$ in each of the layers considered for the Irminger, Iceland and Rockall basins during the period 2009-2019. The sum of changes explained by the individual drivers represents the calculated interannual $pH_T$ change $\left(\frac{dpH_T}{dt}\text{ calculated}\right)$, as detailed in section 2.2.5. The observed interannual $pH_T$ trends $\left(\frac{dpH_T}{dt}\text{ observed}\right)$, shown in Figure 7 and provided in Table 2, were also added to the table for comparison.

1093   Table 4. Temporal changes in $\Omega$Ca and $\Omega$Arag (**in $10^{-3}$ units yr$^{-1}$**) explained by fluctuations in

1094   temperature $\left(\frac{\partial\Omega}{\partial T}\frac{\partial T}{dt}\right)$, salinity $\left(\frac{\partial\Omega}{\partial S}\frac{\partial S}{dt}\right)$, $A_T$ $\left(\frac{\partial\Omega}{\partial A_T}\frac{\partial NA_T}{dt}\right)$, and $C_T$ $\left(\frac{\partial\Omega}{\partial C_T}\frac{\partial NC_T}{dt}\right)$ in each of the layers

1095   considered for the Irminger, Iceland and Rockall basins during the period 2009-2019. The sum

1096   of changes explained by the individual drivers represents the calculated interannual $\Omega$ change

1097   $\left(\frac{d\Omega}{dt}\text{ calculated}\right)$, as detailed in section 2.2.6. The observed interannual $\Omega$ trends

1098   $\left(\frac{d\Omega}{dt}\text{ observed}\right)$, shown in Figure 6 and provided in Table 2, were also added to the table for

1099   comparison.
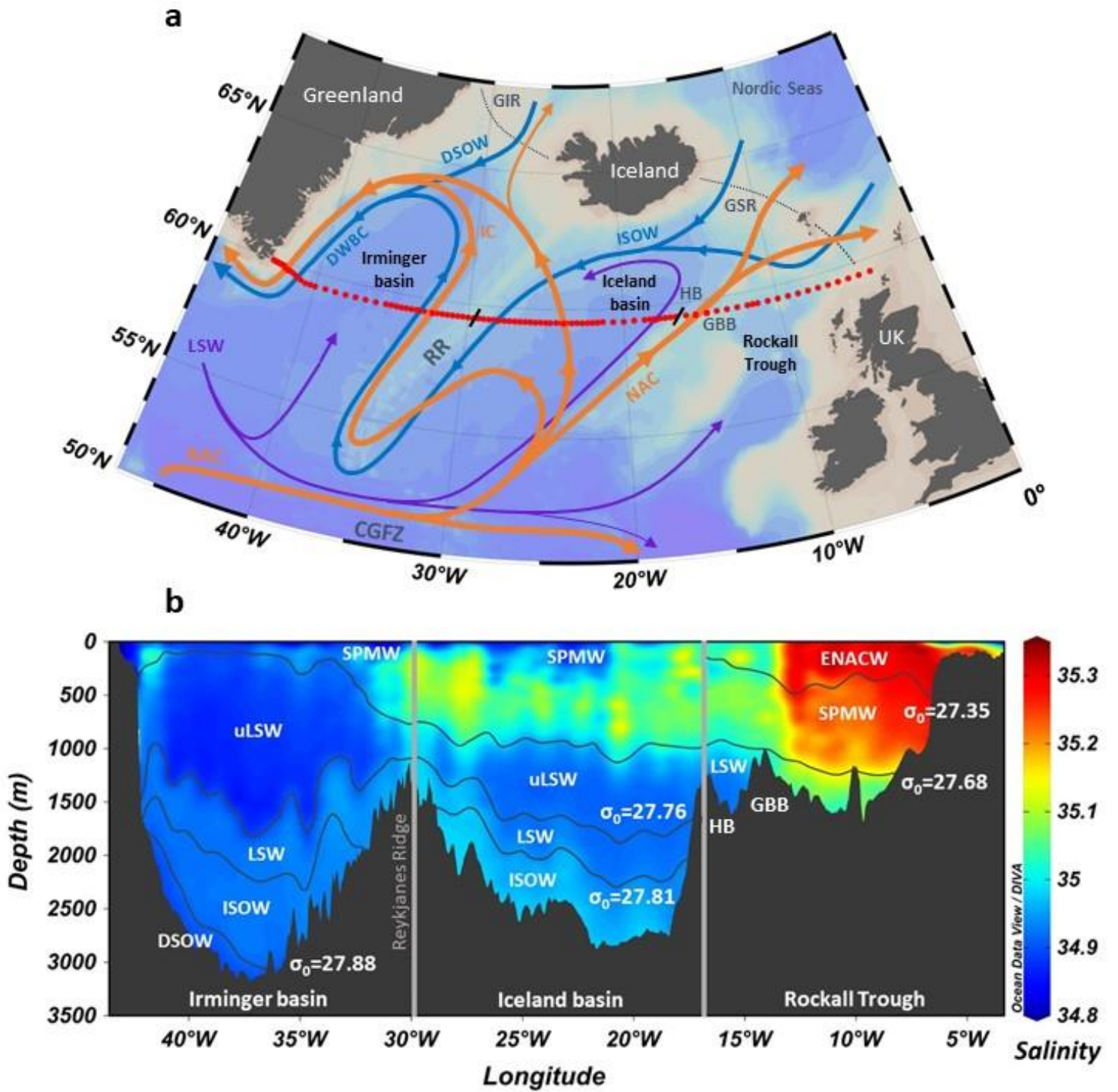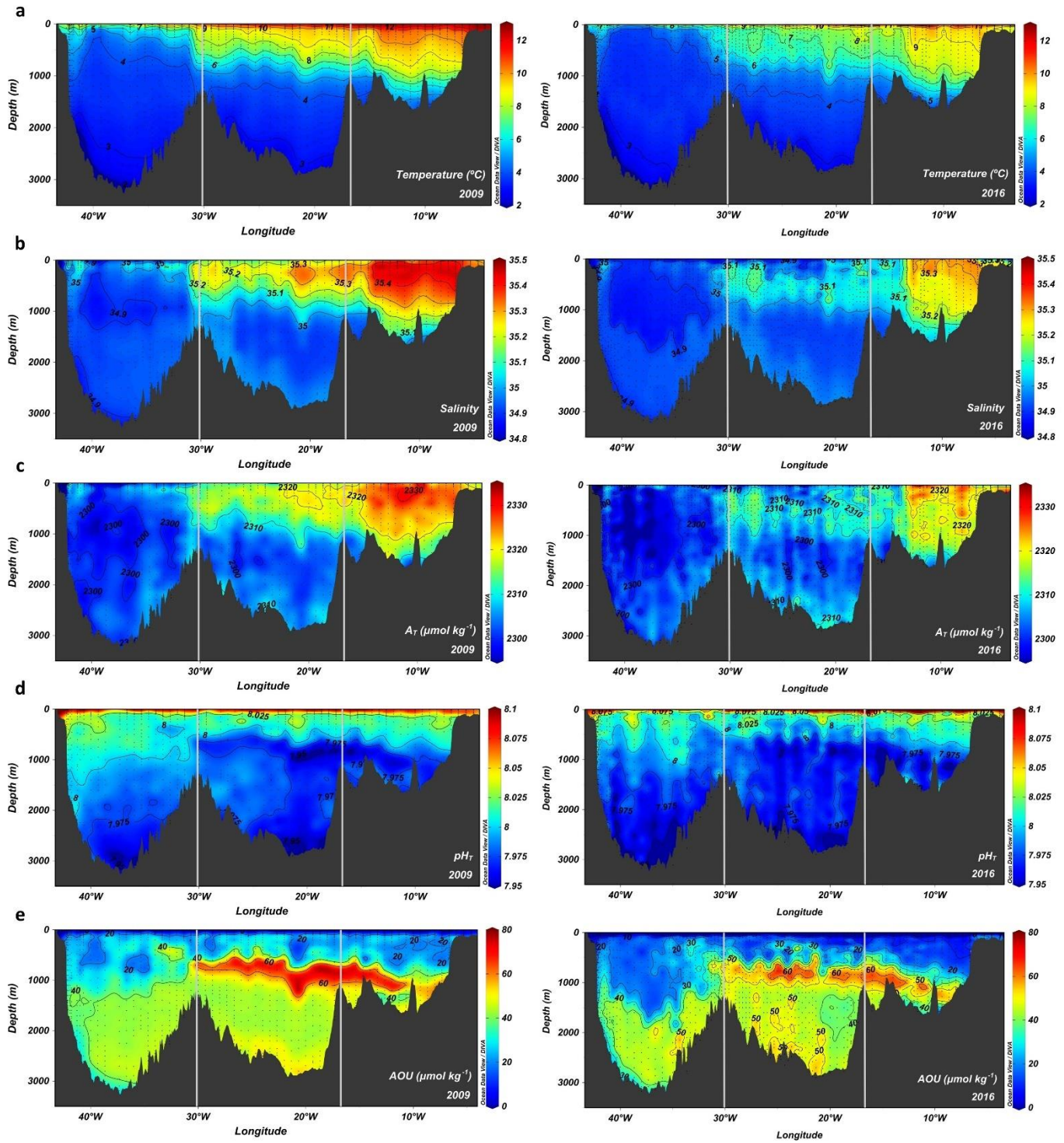
1103    Fig. 3

1104
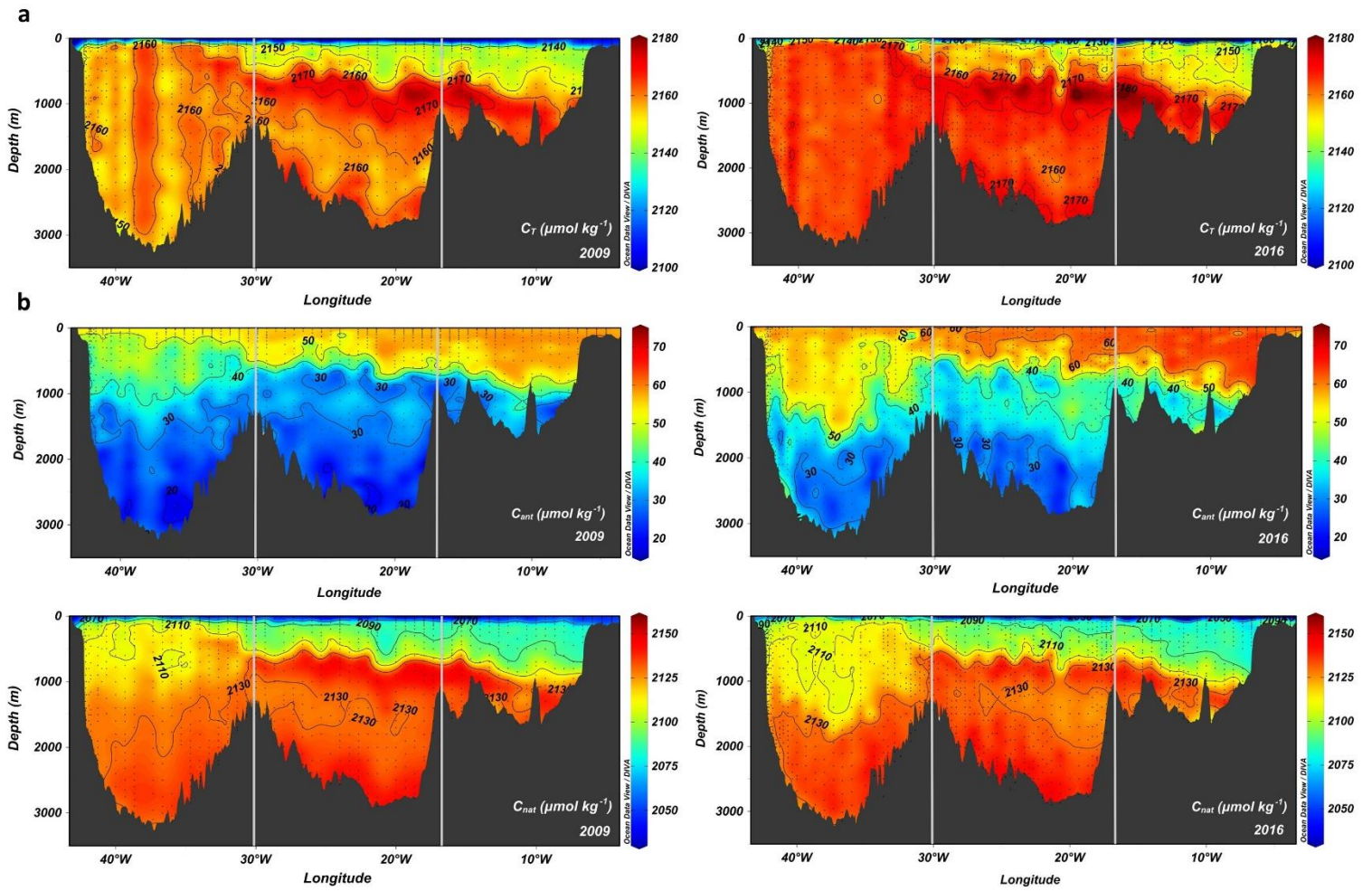
Fig. 4
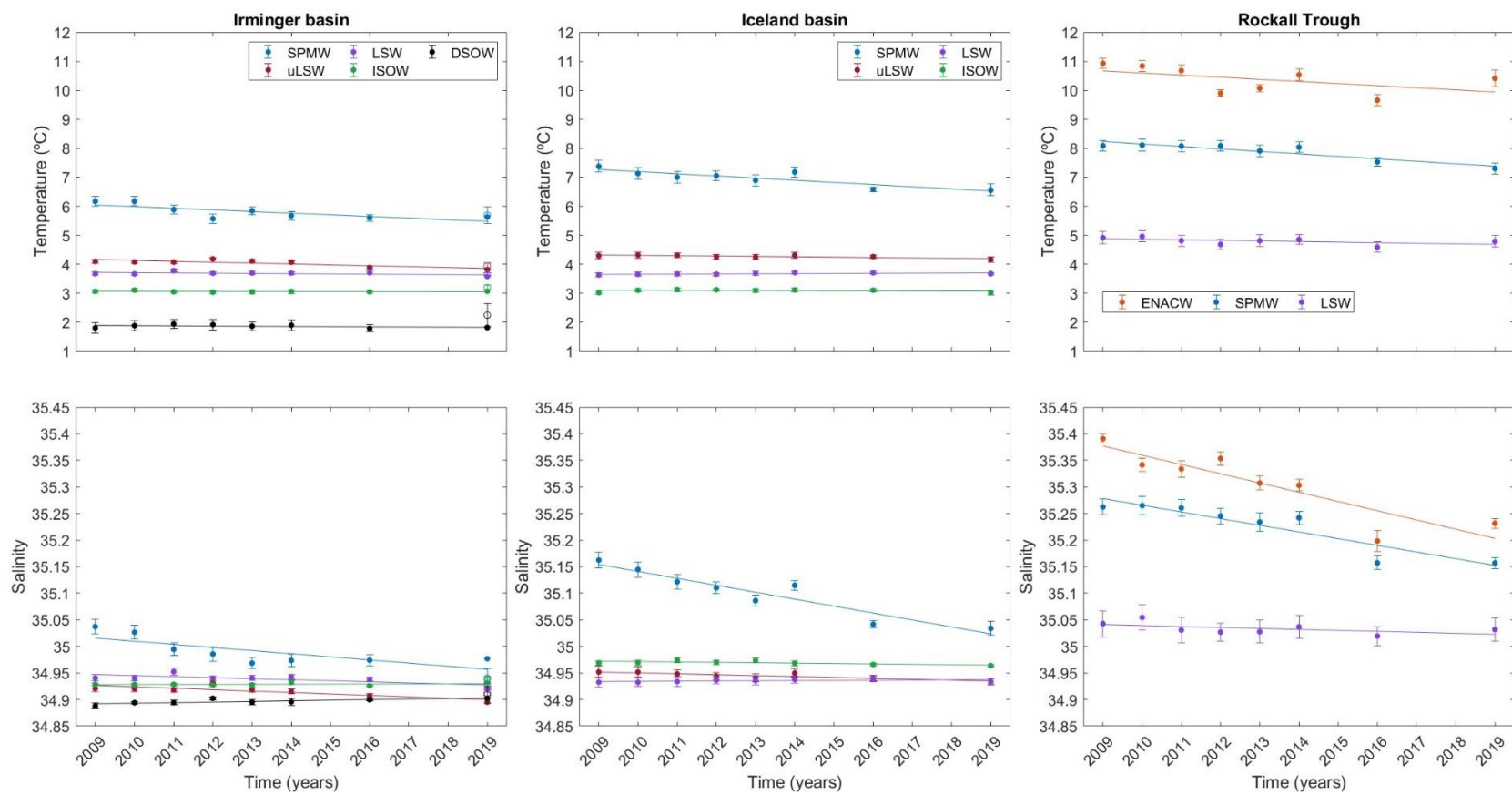
Fig. 5
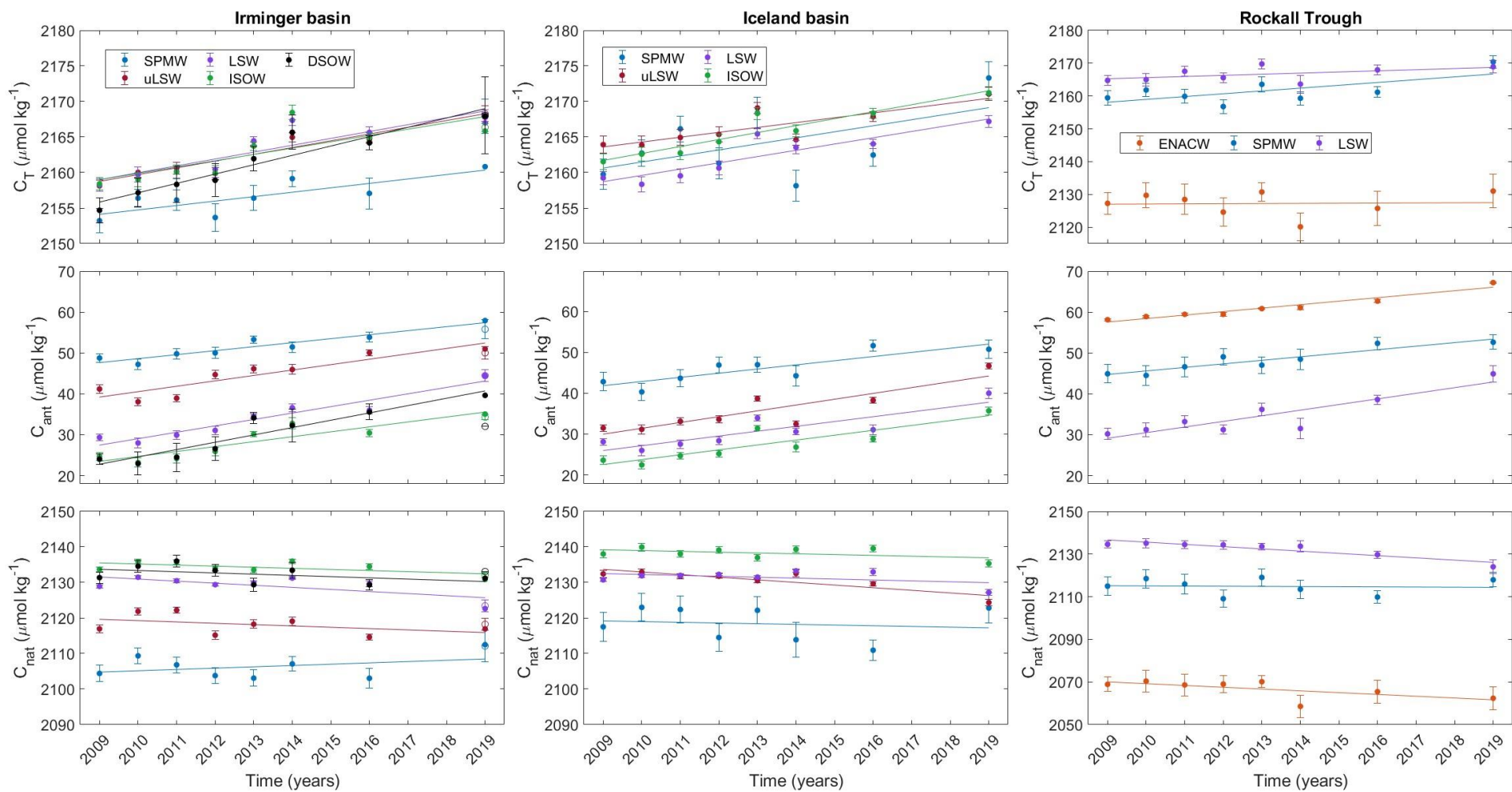
Fig. 6
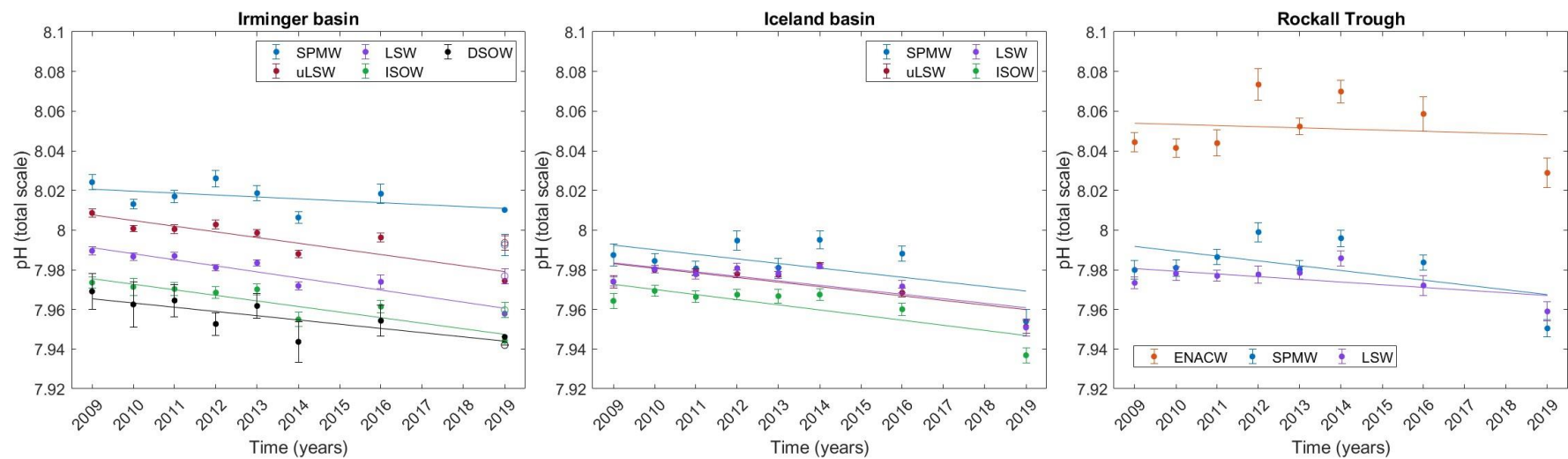
Fig. 7
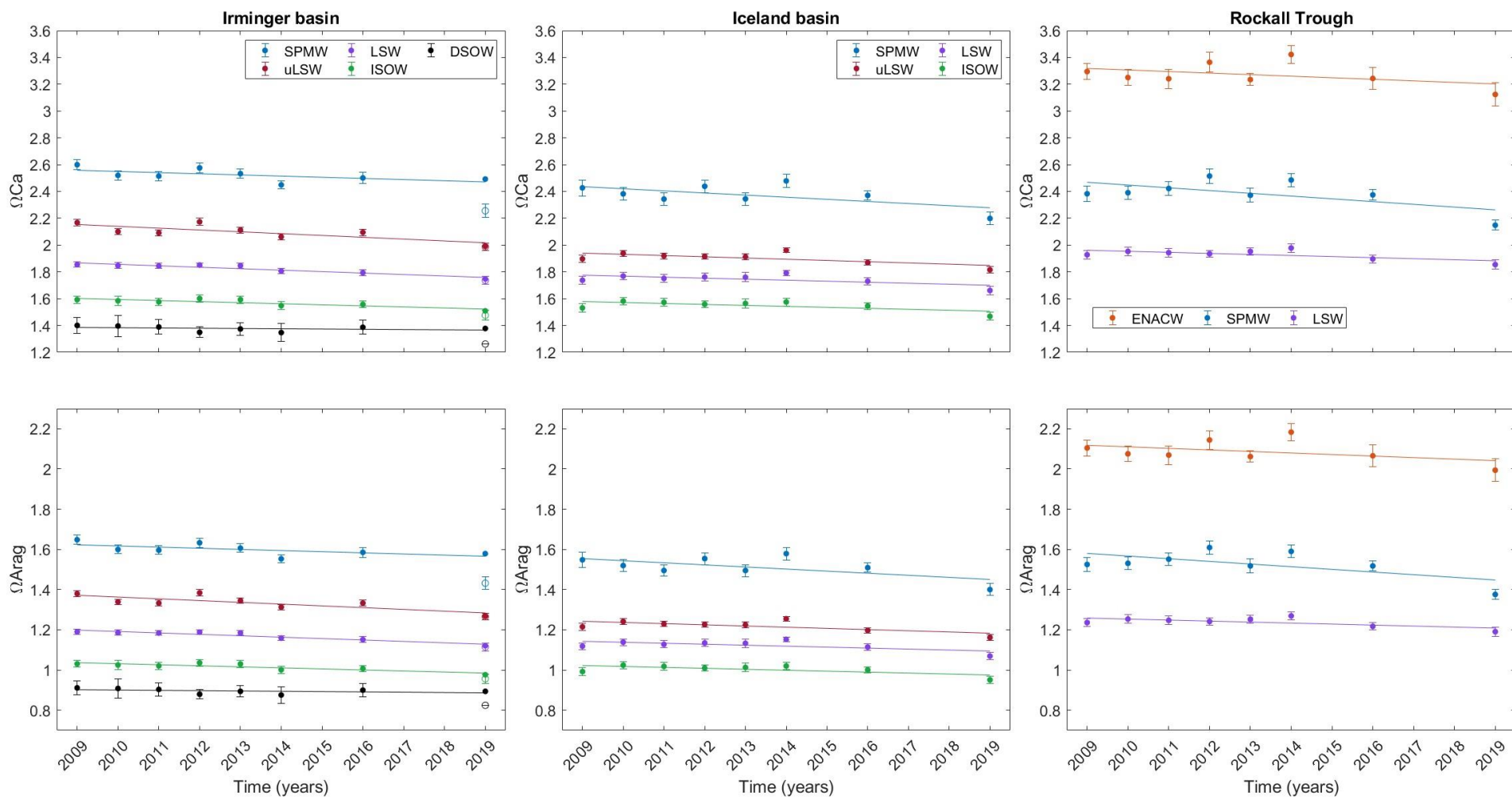
Table 1

| Year | Cruise ID | Date | Research Vessel (R/V) | Chief Scientist | Number of stations | MCS measured variables |
|------|-----------|------|----------------------|-----------------|--------------------|------------------------|
| 2009 | AI28 | Aug 15-Sept 27 | Akademik Ioffe | A. Sokov | 67 | $A_T$, $C_T$ and pH |
| 2010 | AI31 | Sep 2-Sep 27 | Akademik Ioffe | A. Sokov | 84 | $A_T$, $C_T$ and pH |
| 2011 | SV33 | Sep 9-Sep 28 | Akademik Sergey Vavilov | A. Sokov | 98 | $A_T$, $C_T$ and pH |
| 2012 | AI38 | May 25-Jul 1 | Akademik Ioffe | S. Gladyshev | 66 | $A_T$, $C_T$ and pH |
| 2013 | AI41 | Jun 26-Jul 23 | Akademik Ioffe | S. Gladyshev | 75 | $A_T$, $C_T$ and pH |
| 2014 | AI44 | Jun 27-Jul 20 | Akademik Ioffe | S. Gladyshev | 76 | $A_T$, $C_T$ and pH |
| 2016 | AI51 | Jun 3-Jul 13 | Akademik Ioffe | S. Gladyshev | 104 | $A_T$, $C_T$ and pH |
| 2019 | AMK77 | Aug 8-Sep 10 | Akademik Mstislav Keldysh | S. Gladyshev | 47 | $A_T$ and $C_T$ |

Table 2

| Basin | Layer | Temperature | | | Salinity | | | $C_T$ | | | $C_{ant}$ | | | $C_{nat}$ | | | $pH_T$ | | | $\Omega ca$ | | | $\Omega Arag$ | | |
|---|---|---|---|---|---|---|---|---|---|---|---|---|---|---|---|---|---|---|---|---|---|---|---|---|---|
| | | ratio (°C yr$^{-1}$) | r$^2$ | p-value | ratio (psu yr$^{-1}$) | r$^2$ | p-value | ratio (µmol kg$^{-1}$ yr$^{-1}$) | r$^2$ | p-value | ratio (µmol kg$^{-1}$ yr$^{-1}$) | r$^2$ | p-value | ratio (µmol kg$^{-1}$ yr$^{-1}$) | r$^2$ | p-value | ratio (10$^{-3}$ units yr$^{-1}$) | r$^2$ | p-value | ratio (units yr$^{-1}$) | r$^2$ | p-value | ratio (units yr$^{-1}$) | r$^2$ | p-value |
| **Irminger** | **SPMW** | **-0.058 ± 0.024** 0.60 0.02 | | | **-0.006 ± 0.003** 0.59 0.03 | | | **0.62 ± 0.23** 0.66 0.02 | | | **0.95 ± 0.17** 0.89 <0.01 | | | **-1.00 ± 0.42** 0.60 0.02 | | | -1.25 ± 0.93 0.32 0.14 | | | **-0.011 ± 0.006** 0.50 0.05 | | | **-0.007 ± 0.003** 0.53 0.04 | | |
| | **uLSW** | -0.014 ± 0.011 0.30 0.16 | | | **-0.002 ± 0.001** 0.59 0.03 | | | **1.02 ± 0.18** 0.89 <0.01 | | | **1.48 ± 0.29** 0.87 <0.01 | | | -0.47 ± 0.38 0.28 0.18 | | | **-2.62 ± 0.69** 0.79 <0.01 | | | -0.008 ± 0.005 0.40 0.09 | | | -0.006 ± 0.003 0.44 0.08 | | |
| | **LSW** | -0.010 ± 0.008 0.31 0.15 | | | **-0.002 ± 0.001** 0.50 0.05 | | | **0.98 ± 0.26** 0.78 <0.01 | | | **1.53 ± 0.23** 0.92 <0.01 | | | -0.54 ± 0.30 0.46 0.06 | | | **-3.17 ± 0.52** 0.91 <0.01 | | | **-0.014 ± 0.003** 0.85 <0.01 | | | **-0.009 ± 0.002** 0.85 <0.01 | | |
| | **ISOW** | -0.002 ± 0.003 0.11 0.42 | | | 0.000 ± 0.000 0.00 0.99 | | | **0.90 ± 0.34** 0.64 0.02 | | | **1.18 ± 0.29** 0.81 <0.01 | | | -0.27 ± 0.20 0.32 0.14 | | | **-2.97 ± 0.70** 0.83 <0.01 | | | **-0.010 ± 0.003** 0.73 <0.01 | | | **-0.007 ± 0.002** 0.74 <0.01 | | |
| | **DSOW** | -0.008 ± 0.008 0.22 0.25 | | | 0.001 ± 0.001 0.43 0.08 | | | **1.32 ± 0.23** 0.90 <0.01 | | | **1.77 ± 0.32** 0.89 <0.01 | | | -0.32 ± 0.33 0.19 0.28 | | | **-2.41 ± 0.87** 0.67 <0.01 | | | -0.004 ± 0.003 0.39 0.10 | | | -0.003 ± 0.002 0.46 0.07 | | |
| **Iceland** | **SPMW** | **-0.074 ± 0.022** 0.74 <0.01 | | | **-0.013 ± 0.002** 0.89 <0.01 | | | 0.85 ± 0.64 0.32 0.15 | | | **1.02 ± 0.31** 0.74 <0.01 | | | -0.19 ± 0.74 0.02 0.75 | | | -2.32 ± 1.63 0.34 0.13 | | | -0.016 ± 0.010 0.37 0.11 | | | -0.010 ± 0.007 0.39 0.10 | | |
| | **uLSW** | **-0.012 ± 0.005** 0.63 0.02 | | | **-0.002 ± 0.000** 0.76 <0.01 | | | **0.68 ± 0.22** 0.71 <0.01 | | | **1.42 ± 0.38** 0.78 <0.01 | | | **-0.74 ± 0.21** 0.75 <0.01 | | | **-2.31 ± 1.01** 0.58 0.03 | | | -0.009 ± 0.005 0.46 0.07 | | | -0.006 ± 0.003 0.47 0.06 | | |
| | **LSW** | 0.005 ± 0.003 0.43 0.08 | | | 0.000 ± 0.000 0.28 0.18 | | | **0.88 ± 0.22** 0.80 <0.01 | | | **1.18 ± 0.35** 0.75 <0.01 | | | -0.26 ± 0.26 0.20 0.27 | | | **-2.26 ± 1.06** 0.54 0.04 | | | -0.008 ± 0.005 0.41 0.09 | | | -0.005 ± 0.003 0.41 0.09 | | |
| | **ISOW** | -0.003 ± 0.006 0.05 0.61 | | | **-0.001 ± 0.000** 0.47 0.05 | | | **0.98 ± 0.17** 0.89 <0.01 | | | **1.20 ± 0.32** 0.79 <0.01 | | | -0.23 ± 0.21 0.23 0.23 | | | **-2.58 ± 0.99** 0.64 <0.01 | | | -0.007 ± 0.004 0.42 0.08 | | | -0.005 ± 0.003 0.43 0.08 | | |
| **Rockall** | **ENACW** | -0.073 ± 0.061 0.27 0.19 | | | **-0.017 ± 0.004** 0.80 <0.01 | | | 0.05 ± 0.57 0.00 0.92 | | | **0.85 ± 0.11** 0.94 <0.01 | | | -0.84 ± 0.50 0.43 0.08 | | | -0.58 ± 2.31 0.02 0.77 | | | -0.012 ± 0.013 0.18 0.30 | | | -0.008 ± 0.008 0.19 0.28 | | |
| | **SPMW** | **-0.085 ± 0.019** 0.84 <0.01 | | | **-0.013 ± 0.003** 0.85 <0.01 | | | **0.86 ± 0.46** 0.48 0.05 | | | **0.87 ± 0.18** 0.86 <0.01 | | | -0.07 ± 0.59 0.00 0.88 | | | -2.43 ± 1.90 0.30 0.16 | | | -0.021 ± 0.013 0.38 0.10 | | | -0.013 ± 0.008 0.39 0.10 | | |
| | **LSW** | -0.020 ± 0.016 0.29 0.17 | | | -0.002 ± 0.001 0.30 0.16 | | | 0.35 ± 0.29 0.27 0.19 | | | **1.38 ± 0.34** 0.81 <0.01 | | | **-1.05 ± 0.24** 0.84 <0.01 | | | -1.36 ± 0.97 0.34 0.13 | | | -0.008 ± 0.004 0.45 0.07 | | | -0.005 ± 0.003 0.45 0.07 | | |

Table 3

| Basin | Layer | $\frac{\partial pH_T}{\partial T}\frac{\partial T}{dt}$ | $\frac{\partial pH_T}{\partial S}\frac{\partial S}{dt}$ | $\frac{\partial pH_T}{\partial A_T}\frac{\partial NA_T}{dt}$ | $\frac{\partial pH_T}{\partial C_T}\frac{\partial NC_T}{dt}$ | $\frac{dpH_T}{dt}$ (obs) | $\frac{dpH_T}{dt}$ (calculated) |
|---|---|---|---|---|---|---|---|
| Irminger | SPMW | 0.91 ± 0.38 | 0.05 ± 0.02 | 0.31 ± 0.43 | -2.67 ± 0.63 | -1.25 ± 0.93 | -1.41 ± 0.85 |
| | uLSW | 0.22 ± 0.17 | 0.02 ± 0.01 | -0.10 ± 0.40 | -2.99 ± 0.53 | -2.62 ± 0.69 | -2.86 ± 0.68 |
| | LSW | 0.16 ± 0.12 | 0.01 ± 0.01 | -0.04 ± 0.39 | -2.85 ± 0.62 | -3.17 ± 0.52 | -2.72 ± 0.74 |
| | ISOW | 0.03 ± 0.05 | 0.00 ± 0.00 | -0.13 ± 0.30 | -2.38 ± 0.88 | -2.97 ± 0.70 | -2.48 ± 0.93 |
| | DSOW | 0.13 ± 0.12 | -0.01 ± 0.00 | -0.60 ± 0.18 | -3.41 ± 0.62 | -2.41 ± 0.87 | -3.90 ± 0.66 |
| Iceland | SPMW | 1.15 ± 0.35 | 0.10 ± 0.02 | 0.61 ± 0.19 | -4.14 ± 1.76 | -2.32 ± 1.63 | -2.27 ± 1.81 |
| | uLSW | 0.19 ± 0.08 | 0.01 ± 0.00 | -0.24 ± 0.45 | -2.08 ± 0.66 | -2.31 ± 1.01 | -2.12 ± 0.80 |
| | LSW | -0.08 ± 0.05 | 0.00 ± 0.00 | -0.04 ± 0.44 | -2.26 ± 0.57 | -2.26 ± 1.06 | -2.38 ± 0.72 |
| | ISOW | 0.04 ± 0.10 | 0.01 ± 0.00 | 0.12 ± 0.40 | -2.70 ± 0.43 | -2.58 ± 0.99 | -2.53 ± 0.60 |
| Rockall | ENACW | 1.13 ± 0.94 | 0.14 ± 0.04 | 0.73 ± 0.66 | -2.25 ± 1.39 | -0.58 ± 2.31 | -0.25 ± 1.80 |
| | SPMW | 1.31 ± 0.29 | 0.10 ± 0.02 | 0.47 ± 0.22 | -3.84 ± 1.23 | -2.43 ± 1.90 | -1.96 ± 1.28 |
| | LSW | 0.30 ± 0.24 | 0.01 ± 0.01 | -0.14 ± 0.37 | -0.94 ± 0.86 | -1.36 ± 0.97 | -0.76 ± 0.96 |

Table 4

| Basin | Layer | | $\frac{\partial \Omega}{\partial T}\frac{\partial T}{dt}$ | $\frac{\partial \Omega}{\partial S}\frac{\partial S}{dt}$ | $\frac{\partial \Omega}{\partial A_T}\frac{\partial NA_T}{dt}$ | $\frac{\partial \Omega}{\partial C_T}\frac{\partial NC_T}{dt}$ | $\frac{d\Omega}{dt}(obs)$ | $\frac{d\Omega}{dt}(calculated)$ |
|---|---|---|---|---|---|---|---|---|
| Irminger | SPMW | Calcite | -0.57 ± 0.24 | -0.43 ± 0.18 | 1.68 ± 2.37 | -13.35 ± 3.14 | -11.03 ± 5.57 | -12.67 ± 3.94 |
| | | Aragonite | -0.49 ± 0.20 | -0.29 ± 0.12 | 1.07 ± 1.50 | -8.47 ± 1.99 | -7.17 ± 3.46 | -8.17 ± 2.50 |
| | uLSW | Calcite | -0.17 ± 0.13 | -0.12 ± 0.05 | -0.46 ± 1.82 | -12.61 ± 2.24 | -8.28 ± 5.16 | -13.36 ± 2.89 |
| | | Aragonite | -0.13 ± 0.10 | -0.08 ± 0.03 | -0.29 ± 1.16 | -8.03 ± 1.43 | -5.55 ± 3.21 | -8.53 ± 1.84 |
| | LSW | Calcite | -0.15 ± 0.11 | -0.09 ± 0.05 | -0.17 ± 1.55 | -10.42 ± 2.27 | -13.54 ± 2.88 | -10.83 ± 2.75 |
| | | Aragonite | -0.11 ± 0.08 | -0.06 ± 0.03 | -0.11 ± 0.99 | -6.69 ± 1.45 | -8.65 ± 1.83 | -6.97 ± 1.76 |
| | ISOW | Calcite | -0.04 ± 0.05 | 0.00 ± 0.01 | -0.44 ± 1.03 | -7.48 ± 2.75 | -10.35 ± 3.23 | -7.96 ± 2.94 |
| | | Aragonite | -0.02 ± 0.04 | 0.00 ± 0.01 | -0.29 ± 0.67 | -4.84 ± 1.78 | -6.66 ± 2.04 | -5.15 ± 1.90 |
| | DSOW | Calcite | -0.13 ± 0.12 | 0.03 ± 0.02 | -1.78 ± 0.52 | -9.23 ± 1.68 | -4.30 ± 2.76 | -11.11 ± 1.77 |
| | | Aragonite | -0.09 ± 0.09 | 0.02 ± 0.01 | -1.16 ± 0.34 | -6.01 ± 1.10 | -3.02 ± 1.68 | -7.24 ± 1.15 |
| Iceland | SPMW | Calcite | -0.88 ± 0.26 | -0.86 ± 0.16 | 3.16 ± 1.00 | -19.59 ± 8.35 | -15.77 ± 10.40 | -18.17 ± 8.42 |
| | | Aragonite | -0.72 ± 0.22 | -0.58 ± 0.10 | 2.02 ± 0.64 | -12.48 ± 5.32 | -10.37 ± 6.55 | -11.77 ± 5.37 |
| | uLSW | Calcite | -0.17 ± 0.07 | -0.09 ± 0.03 | -1.02 ± 1.89 | -7.98 ± 2.52 | -9.18 ± 5.11 | -9.26 ± 3.15 |
| | | Aragonite | -0.12 ± 0.05 | -0.06 ± 0.02 | -0.65 ± 1.21 | -5.11 ± 1.61 | -5.92 ± 3.23 | -5.95 ± 2.02 |
| | LSW | Calcite | 0.08 ± 0.05 | 0.02 ± 0.01 | -0.15 ± 1.70 | -7.92 ± 2.00 | -7.53 ± 4.64 | -7.97 ± 2.63 |
| | | Aragonite | 0.06 ± 0.03 | 0.01 ± 0.01 | -0.09 ± 1.09 | -5.10 ± 1.29 | -4.83 ± 2.96 | -5.12 ± 1.69 |
| | ISOW | Calcite | -0.04 ± 0.10 | -0.03 ± 0.02 | 0.41 ± 1.37 | -8.38 ± 1.33 | -7.22 ± 4.34 | -8.05 ± 1.91 |
| | | Aragonite | -0.03 ± 0.07 | -0.02 ± 0.01 | 0.27 ± 0.89 | -5.43 ± 0.86 | -4.72 ± 2.76 | -5.22 ± 1.24 |
| Rockall | ENACW | Calcite | -0.82 ± 0.69 | -1.50 ± 0.38 | 5.16 ± 4.63 | -14.21 ± 8.78 | -11.60 ± 12.67 | -11.37 ± 9.95 |
| | | Aragonite | -0.79 ± 0.66 | -1.00 ± 0.25 | 3.29 ± 2.95 | -9.06 ± 5.60 | -7.66 ± 7.96 | -7.57 ± 6.37 |
| | SPMW | Calcite | -1.15 ± 0.26 | -0.82 ± 0.18 | 2.44 ± 1.15 | -18.21 ± 5.83 | -20.57 ± 13.40 | -17.74 ± 5.95 |
| | | Aragonite | -0.93 ± 0.21 | -0.55 ± 0.12 | 1.56 ± 0.74 | -11.66 ± 3.73 | -13.24 ± 8.47 | -11.58 ± 3.81 |
| | LSW | Calcite | -0.28 ± 0.22 | -0.10 ± 0.08 | -0.58 ± 1.57 | -3.62 ± 3.30 | -7.88 ± 4.41 | -4.59 ± 3.66 |
| | | Aragonite | -0.21 ± 0.16 | -0.07 ± 0.05 | -0.37 ± 1.01 | -2.33 ± 2.12 | -4.97 ± 2.82 | -2.97 ± 2.35 |

# References

Accornero, A., Manno, C., Esposito, F., & Gambi, M.C. (2003). The vertical flux of particulate matter in the polynya of Terra Nova Bay. Part II. Biological components. Antarctic Science, 15, 175–188. DOI: 10.1017/S0954102003001214

Álvarez, M., Pérez, F.F., Bryden, H., & Ríos, A.F. (2004). Physical and biogeochemical transports structure in the North Atlantic subpolar gyre. Journal of Geophysical Research: Ocean, 109. DOI: 10.1029/2003jc002015

Álvarez, M., Ríos, A.F., Pérez, F.F., Bryden, H.L., & Rosón, G. (2003). Transports and budgets of total inorganic carbon in the subpolar and temperate North Atlantic. Global Biogeochemical Cycles, 17(2), 2-1-2–21. DOI: 10.1029/2002gb001881

Anderson, L.G. (2001). of the Surface Ocean CO2 System in the Nordic Seas and Northern North Atlantic to Climate Change Using mixed-layer salinity and temperature Model and empirical relationships between sea surface temperature and surface water CO2 fugacity, and between sea.

Azetsu-Scott, K., Jones, E. P., Yashayaev, I., & Gershey, R. M. (2003). Time series study of CFC concentrations in the Labrador Sea during deep and shallow convection regimes (1991–2000). Journal of Geophysical Research: Oceans, 108(C11).

Balmaseda, M.A., Smith, G.C., Haines, K., Anderson, D., Palmer, T.N., & Vidard, A. (2007). Historical reconstruction of the Atlantic Meridional Overturning Circulation from the ECMWF operational ocean reanalysis. Geophysical Research Letters, 34, 1–6. DOI: 10.1029/2007GL031645

Bates, N.R., Astor, Y.M., Church, M.J., Currie, K., Dore, J.E., González-Dávila, M., Lorenzoni, L., Muller-Karger, F., Olafsson, J., & Santana-Casiano, J.M. (2014). A time-series view of changing surface ocean chemistry due to ocean uptake of anthropogenic CO2 and ocean acidification. Oceanography, 27, 126–141. DOI: 10.5670/oceanog.2014.16

Bates, N.R., Best, M.H.P., Neely, K., Garley, R., Dickson, A.G., & Johnson, R.J. (2012). Detecting anthropogenic carbon dioxide uptake and ocean acidification in the North Atlantic Ocean. Biogeosciences, 9, 2509–2522. DOI: 10.5194/bg-9-2509-2012

Bathmann, U. V., Noji, T.T., & von Bodungen, B. (1991). Sedimentation of pteropods in the Norwegian Sea in autumn. Deep Sea Research Part A. Oceanographic Research Papers, 38, 1341–1360. DOI: 10.1016/0198-0149(91)90031-A

Benson, B.B., & Krause, D. (1984). The concentration and isotopic fractionation of oxygen dissolved in freshwater and seawater in equilibrium with the atmosphere. Deep Sea Research Part B. Oceanographic Literature Review, 31, 859. DOI: 10.1016/0198-0254(84)93289-8

Bersch, M., Yashayaev, I., & Koltermann, K. P. (2007). Recent changes of the thermohaline circulation in the subpolar North Atlantic. Ocean Dynamics, 57, 223-235.

Bittig, H.C., Steinhoff, T., Claustre, H., Fiedler, B., Williams, N.L., Sauzède, R., Körtzinger, A., & Gattuso, J.P. (2018). An alternative to static climatologies: Robust estimation of open ocean $CO_2$ variables and nutrient concentrations from T, S, and $O_2$ data using Bayesian neural networks. Frontiers in Marine Science, 5, 1–29. DOI: 10.3389/fmars.2018.00328

Böning, C.W., Scheinert, M., Dengg, J., Biastoch, A., & Funk, A. (2006). Decadal variability of subpolar gyre transport and its reverberation in the North Atlantic overturning. Geophysical Research Letters, 33. DOI: 10.1029/2006GL026906

Brambilla, E., & Talley, L.D. (2008). Subpolar mode water in the northeastern Atlantic: 1. Averaged properties and mean circulation. Journal of Geophysical Research: Ocean, 113, 1–18. DOI: 10.1029/2006JC004062

Broecker, W.S., & Peng, T.H. (1983). Tracers in the sea: W. S. Broecker and T. H. Peng. Eldigio Press Lamont Doherty Geological Observatory, 1982, 690 pages (300 figures and tables; 740 commented bibliographic references), US $35.00. Geochimica et Cosmochimica Acta, 47, 1336. DOI: 10.1016/0016-7037(83)90075-3

Bryden, H.L., King, B.A., Mccarthy, G.D., & Mcdonagh, E.L. (2014). Impact of a 30 % reduction in Atlantic meridional overturning during 2009 – 2010 683–691. DOI: 10.5194/os-10-683-2014

Caldeira, K., & Wickett, M. (2005). Ocean model predictions of chemistry changes from carbon dioxide emissions to the atmosphere and ocean. Journal of Geophysical Research C: Oceans, 110, 1–12. DOI: 10.1029/2004JC002671

Caldeira, K., & Wickett, M.E. (2003). Anthropogenic carbon and ocean pH. Nature, 425, 365. DOI: 10.1038/425365a

Carpenter, J. H. (1965). The accuracy of the Winkler method for dissolved oxygen analysis 1. Limnology and Oceanography, 10(1), 135-140.

Carrit, D. E., & Carpenter, J. H. (1966). Recommendation procedure for Winkler analyses of sea water for dissolved oxygen. Journal of Marine Research, 24, 313-318.

Carter, B.R., Bittig, H.C., Fassbender, A.J., Sharp, J.D., Takeshita, Y., Xu, Y.Y., Álvarez, M., Wanninkhof, R., Feely, R.A., & Barbero, L. (2021). New and updated global empirical seawater property estimation routines. Limnology and Oceanography: Methods, 19, 785–809. DOI: 10.1002/lom3.10461

Chau, T.-T.-T., Gehlen, M., Metzl, N., and Chevallier, F.: CMEMS-LSCE: a global, 0.25°, monthly reconstruction of the surface ocean carbonate system, Earth Syst. Sci. Data, 16, 121–160, https://doi.org/10.5194/essd-16-121-2024, 2024.

Clayton, T.D., & Byrne, R.H. (1993). Spectrophotometric seawater pH measurements: total hydrogen ion concentration scale calibration of m-cresol purple and at-sea results. Deep

Sea Research Part I: Oceanographic Research Papers, 40, 2115–2129. DOI: 10.1016/0967-0637(93)90048-8

Collier, R., Dymond, J., Honjo, S., Manganini, S., Francois, R., & Dunbar, R. (2000). The vertical flux of biogenic and lithogenic material in the Ross Sea: Moored sediment trap observations 1996-1998. Deep Sea Research Part II: Topical Studies in Oceanography, 47, 3491–3520. DOI: 10.1016/S0967-0645(00)00076-X

Corbière, A., Metzl, N., Reverdin, G., Brunet, C., & Takahashi, T. (2007). Interannual and decadal variability of the oceanic carbon sink in the North Atlantic subpolar gyre. Tellus, Series B: Chemical and Physical Meteorology, 59, 168–178. DOI: 10.1111/j.1600-0889.2006.00232.x

Daniault, N., Mercier, H., Lherminier, P., Sarafanov, A., Falina, A., Zunino, P., Pérez, F.F., & Ríos, A.F. (2016). The northern North Atlantic Ocean mean circulation in the early 21st century. Progress in Oceanography, 146, 142–158. DOI: 10.1016/j.pocean.2016.06.007

de la Paz, M., García-Ibáñez, M. I., Steinfeldt, R., Ríos, A. F., & Pérez, F. F. (2017). Ventilation versus biology: What is the controlling mechanism of nitrous oxide distribution in the North Atlantic?. Global Biogeochemical Cycles, 31(4), 745–760. DOI: 10.1002/2016GB005507

Dickson, A. D. 1995. Determination of dissolved oxygen in sea water by Winkler titration. WOCE Operations Manual, Part 3.1.3 Operations & Methods, WHP Office Report WHPO 91-1.

Dickson, A. G., & Goyet, C. (1994). Handbook of methods for the analysis of the various parameters of the carbon dioxide system in sea water. V. 2. United States. DOI: 10.2172/10107773

Dickson, A. G., Sabine, C. L., & Christian, J. R. (2007). Guide to best practices for ocean CO2 measurements. PICES Special Publication 3, 191 pp.

Dickson, B., Yashayaev, I., Meincke, J., Turrell, B., Dye, S., & Holfort, J. (2002). Rapid freshening of the deep North Atlantic Ocean over the past four decades. Nature, 416(6883), 832-837. DOI: 10.1038/416832a

De Jong, M. F., & de Steur, L. (2016). Strong winter cooling over the Irminger Sea in winter 2014–2015, exceptional deep convection, and the emergence of anomalously low SST. Geophysical Research Letters, 43, 7106–7113. DOI: 10.1002/2016GL069596

De Jong, M. F., Van Aken, H. M., Våge, K., & Pickart, R. S. (2012). Convective mixing in the central Irminger Sea: 2002-2010. Deep Sea Research Part I: Oceanographic Research Papers, 63, 36–51. DOI: 10.1016/j.dsr.2012.01.003

DelValls, T. A., & Dickson, A. G. (1998). The pH of buffers based on 2-amino-2-hydroxymethyl-1,3-propanediol ('tris') in synthetic sea water. Deep Sea Research Part I: Oceanographic Research Papers, 45, 1541–1554. DOI: 10.1016/S0967-0637(98)00019-3

Desbruyères, D., Thierry, V., & Mercier, H. (2013). Simulated decadal variability of the meridional overturning circulation across the A25-Ovide section, 462–475. DOI: 10.1029/2012JC008342

Dickson, A. G. (1990). Standard potential of the reaction: AgCl(s) + 1/2H2(g) = Ag(s) + HCl(aq), and the standard acidity constant of the ion HSO4- in synthetic sea water from 273.15 to 318.15 K. J. Chem. Thermodyn., 22, 113–127. DOI: 10.1016/0021-9614(90)90074-Z

Dickson, A. G., & Millero, F. J. (1987). A comparison of the equilibrium constants for the dissociation of carbonic acid in seawater media. Deep Sea Research Part A: Oceanographic Research Papers, 34, 1733–1743. DOI: 10.1016/0198-0149(87)90021-5

Dickson, R. R., & Brown, J. (1994). The production of North Atlantic Deep Water: Sources, rates, and pathways. J. Geophys. Res. Ocean., 99, 12319–12341. DOI: 10.1029/94JC00530

Doney, S. C., Fabry, V. J., Feely, R. A., & Kleypas, J. A. (2009). Ocean Acidification: The Other CO2 Problem. Ann. Rev. Mar. Sci., 1, 169–192. DOI: 10.1146/annurev.marine.010908.163834

Eden, C., & Willebrand, J. (2001). Mechanism of interannual to decadal variability of the North Atlantic circulation. J. Clim., 14, 2266–2280. DOI: 10.1175/1520-0442(2001)014<2266:MOITDV>2.0.CO;2

Ellett, D. J., Edwards, A., & Bowers, R. (1986). The hydrography of the Rockall Channel—an overview. Proc. R. Soc. Edinburgh. Sect. B. Biol. Sci., 88, 61–81. DOI: 10.1017/s0269727000004474

Feely, R. A., Sabine, C. L., Lee, K., Berelson, W., Kleypas, J., Fabry, V. J., Millero, F. J. (2004). Impact of anthropogenic CO2 on the CaCO3 system in the oceans. Science, 305, 362–366. DOI: 10.1126/SCIENCE.1097329

Ferron, B., Kokoszka, F., Mercier, H., Lherminier, P. (2014). Dissipation rate estimates from microstructure and finescale internal wave observations along the A25 Greenland-Portugal OVIDE line. J. Atmos. Ocean. Technol., 31, 2530–2543. DOI: 10.1175/JTECH-D-14-00036.1

Fogelqvist, E., Blindheim, J., Tanhua, T., Østerhus, S., Buch, E., & Rey, F. (2003). Greenland–Scotland overflow studied by hydro-chemical multivariate analysis. Deep Sea Research Part I: Oceanographic Research Papers, 50(1), 73-102.

Fontela, M., Pérez, F. F., Carracedo, L. I., Padín, X. A., Velo, A., García-Ibañez, M. I., Lherminier, P. (2020). The Northeast Atlantic is running out of excess carbonate in the horizon of cold-water corals communities. Sci. Rep., 10. DOI: 10.1038/s41598-020-71793-2

Friedlingstein, P., Sullivan, M. O., Jones, M. W., Andrew, R. M., Gregor, L., Hauck, J., Quéré, C. Le, Luijkx, I. T., Olsen, A., Peters, G. P., Peters, W. (2022). Global Carbon Budget 2022, 4811–4900.

Fröb, F., Olsen, A., Becker, M., Chafik, L., Johannessen, T., Reverdin, G., Omar, A. (2019). Wintertime fCO2 Variability in the Subpolar North Atlantic Since 2004. Geophys. Res. Lett., 46, 1580–1590. DOI: 10.1029/2018GL080554

Fröb, F., Olsen, A., Våge, K., Moore, G. W. K., Yashayaev, I., Jeansson, E., Rajasakaren, B. (2016). Irminger Sea deep convection injects oxygen and anthropogenic carbon to the ocean interior. Nat. Commun., 7. DOI: 10.1038/ncomms13244

García-Ibáñez, M. I., Bates, N. R., Bakker, D. C. E., Fontela, M., Velo, A. (2021). Cold-water corals in the Subpolar North Atlantic Ocean exposed to aragonite undersaturation if the 2 °C global warming target is not met. Global Planetary Change, 201. DOI: 10.1016/j.gloplacha.2021.103480

García-Ibáñez, M. I., Pardo, P. C., Carracedo, L. I., Mercier, H., Lherminier, P., Ríos, A. F., Pérez, F. F. (2015). Structure, transports and transformations of the water masses in the Atlantic Subpolar Gyre. Progress in Oceanography, 135, 18-36. DOI: 10.1016/j.pocean.2015.03.009

García-Ibáñez, M. I., Pérez, F. F., Lherminier, P., Zunino, P., Mercier, H., Tréguer, P. (2018). Water mass distributions and transports for the 2014 GEOVIDE cruise in the North Atlantic. Biogeosciences, 15, 2075-2090. DOI: 10.5194/bg-15-2075-2018

García-Ibáñez, M. I., Zunino, P., Fröb, F., Carracedo, L. I., Ríos, A. F., Mercier, H., Olsen, A., Pérez, F. F. (2016). Ocean acidification in the subpolar North Atlantic: Rates and mechanisms controlling pH changes. Biogeosciences, 13, 3701-3715. DOI: 10.5194/bg-13-3701-2016

Gehlen, M., Séférian, R., Jones, D. O. B., Roy, T., Roth, R., Barry, J., Bopp, L., Doney, S. C., Dunne, J. P., Heinze, C., Joos, F., Orr, J. C., Resplandy, L., Segschneider, J., and Tjiputra, J.: Projected pH reductions by 2100 might put deep North Atlantic biodiversity at risk, Biogeosciences, 11, 6955-6967, 10.5194/bg-11-6955-2014, 2014.

Gladyshev, S. V., Gladyshev, V. S., Falina, A. S., Sarafanov, A. A. (2016a). Winter convection in the Irminger Sea in 2004–2014. Oceanology, 56, 326-335. DOI: 10.1134/S0001437016030073

Gladyshev, S. V., Gladyshev, V. S., Gulev, S. K., Sokov, A. V. (2016b). Anomalously deep convection in the Irminger Sea during the winter of 2014–2015. Doklady Earth Sciences, 469, 766-770. DOI: 10.1134/S1028334X16070229

Gladyshev, S. V., Gladyshev, V. S., Member, C., Gulev, R. A. S. S. K., Sokov, A. V. (2018). Structure and Variability of the Meridional Overturning Circulation in the North Atlantic Subpolar Gyre, 2007–2017. Doklady Earth Sciences, 483, 1524-1527. DOI: 10.1134/S1028334X18120024

Gladyshev, S. V., Gladyshev, V. S., Member, C., Gulev, R. A. S. S. K., Sokov, A. V. (2017). Subpolar Mode Water Classes in the Northeast Atlantic: Interannual and Long-Term Variability. Doklady Earth Sciences, 476, 1203-1206. DOI: 10.1134/S1028334X17100166

González-Dávila, M., & Santana-Casiano, J. M. (2023). Long-term trends of pH and inorganic carbon in the Eastern North Atlantic: the ESTOC site. *Frontiers in Marine Science*, *10*, 1236214.

González-Dávila, M., Santana-Casiano, J. M., Petihakis, G., Ntoumas, M., Suárez de Tangil, M., Krasakopoulou, E. (2016). Seasonal pH variability in the Saronikos Gulf: A year-study using a new photometric pH sensor. Journal of Marine Systems, 162, 37-46. DOI: 10.1016/j.jmarsys.2016.03.007

González-Dávila, M., Santana-Casiano, J. M., Prêcheur-Massieu, H. (2014). New pH sensor for monitoring ocean acidification. Sea Technology, 55, 36-40.

González-Dávila, M., Santana-Casiano, J.M., Rueda, M.J., Llinás, O. (2010). The water column distribution of carbonate system variables at the ESTOC site from 1995 to 2004. Biogeosciences, 7, 3067-3081. DOI: 10.5194/bg-7-3067-2010

Gruber, N., Clement, D., Carter, B.R., Feely, R.A., van Heuven, S., Hoppema, M., Ishii, M., Key, R.M., Kozyr, A., Lauvset, S.K., Monaco, C. Lo, Mathis, J.T., Murata, A., Olsen, A., Perez, F.F., Sabine, C.L., Tanhua, T., Wanninkhof, R. (2019a). The oceanic sink for anthropogenic CO2 from 1994 to 2007. Science, 363, 1193

Gruber, N., Sarmiento, J.L., Stocker, T.F. (1996). An improved method for detecting anthropogenic CO2 in the oceans. Global Biogeochem. Cycles. https://doi.org/10.1029/96GB01608

Guallart, E.F., Fajar, N.M., Padín, X.A., Vázquez-Rodríguez, M., Calvo, E., Ríos, A.F., Hernández-Guerra, A., Pelejero, C., Pérez, F.F. (2015). Ocean acidification along the 24.5°N section in the subtropical North Atlantic. Geophys. Res. Lett., 42, 450–458. https://doi.org/10.1002/2014GL062971

Häkkinen, S. (2002). Surface salinity variability in the northern North Atlantic during recent decades. J. Geophys. Res. Ocean, 107, SRF 4-1. https://doi.org/10.1029/2001JC000812

Häkkinen, S., Rhines, P.B. (2004). Decline of Subpolar North Atlantic Circulation during the 1990s. Science (80-. ), 304, 555–559. https://doi.org/10.1126/science.1094917

Harvey, J. (1982). Theta–S relationships and water masses in the eastern North Atlantic. Deep-Sea Res. Part a-Oceanogr. Res. Pap., 29 (8), 1021–1033.

Hátún, H., Sande, A.B., Drange, H., Hansen, B., Valdimarsson, H. (2005). Influence of the Atlantic subpolar gyre on the thermohaline circulation. Science (80-. ), 309, 1841–1844. https://doi.org/10.1126/science.1114777

Holliday, N.P., Bersch, M., Berx, B., Chafik, L., Cunningham, S., Florindo-López, C., Hátún, H., Johns, W., Josey, S.A., Larsen, K.M.H., Mulet, S., Oltmanns, M., Reverdin, G., Rossby, T., Thierry, V., Valdimarsson, H., Yashayaev, I. (2020). Ocean circulation causes the largest freshening event for 120 years in eastern subpolar North Atlantic. Nat. Commun., 11. https://doi.org/10.1038/s41467-020-14474-y

Holliday, P. N., Pollard, R.T., Read, J.F., Leach, H. (2000). Water mass properties and fluxes in the Rockall Trough, 1975-1998. Deep-Sea Research Part I: Oceanographic Research Papers. https://doi.org/10.1016/S0967-0637(99)00109-0

Humphreys, M. P., et al. (2016). Multidecadal accumulation of anthropogenic and remineralized dissolved inorganic carbon along the Extended Ellett Line in the northeast Atlantic Ocean. Global Biogeochem. Cycles. 30, 293–310, doi:10.1002/2015GB005246.

IPCC. (2013). Climate Change 2013: The Physical Science Basis. Contribution of Working Group I to the Fifth Assessment Report of the Intergovernmental Panel on Climate Change. Cambridge University Press.

IPCC. (2021). Climate Change 2021: The Physical Science Basis. Contribution of Working Group I to the Sixth Assessment Report of the Intergovernmental Panel on Climate Change. Cambridge University Press.

Jackson, L.C., Biastoch, A., Buckley, M.W., Desbruyères, D. G., Frajka-Williams, E., Moat, B., and Robson, J. (2022). The evolution of the North Atlantic Meridional Overturning Circulation since 1980. Nat. Rev. Earth Environ. 3, 241–254. https://doi.org/10.1038/s43017-022-00263-2

Jiang, L.Q., Feely, R.A., Carter, B.R., Greeley, D.J., Gledhill, D.K., Arzayus, K.M. (2015). Climatological distribution of aragonite saturation state in the global oceans. Global Biogeochem. Cycles, 29, 1656–1673. https://doi.org/10.1002/2015GB005198

Johnson, K.M., Wills, K.D., Butler, D.B., Johnson, W.K., Wong, C.S. (1993). Coulometric total carbon dioxide analysis for marine studies: maximizing the performance of an automated gas extraction system and coulometric detector. Mar. Chem., 44, 167–187. https://doi.org/10.1016/0304-4203(93)90201-X

Josey, S.A., Hirschi, J.J.M., Sinha, B., Duchez, A., Grist, J.P., Marsh, R. (2018). The recent Atlantic cold anomaly: Causes, consequences, and related phenomena. Ann. Rev. Mar. Sci., 10, 475–501. https://doi.org/10.1146/annurev-marine-121916-063102

Jung, T., Vitart, F., Ferranti, L., and Morcrette, J. J. (2011). Origin and predictability of the extreme negative NAO winter of 2009/10. Geophysical Research Letters, 38(7).

Khatiwala, S., Tanhua, T., Mikaloff Fletcher, S., Gerber, M., Doney, S.C., Graven, H.D., Gruber, N., McKinley, G.A., Murata, A., Ríos, A.F., Sabine, C.L. (2013). Global ocean storage of anthropogenic carbon. Biogeosciences, 10, 2169–2191. https://doi.org/10.5194/bg-10-2169-2013

Kieke, D., Rhein, M., Stramma, L., Smethie, W. M., Bullister, J. L., & LeBel, D. A. (2007). Changes in the pool of Labrador Sea Water in the subpolar North Atlantic. Geophysical Research Letters, 34(6).

Knight, J.R., Folland, C.K., Scaife, A.A. (2006). Climate impacts of the Atlantic multidecadal oscillation. Geophys. Res. Lett., 33, 2–5. https://doi.org/10.1029/2006GL026242

Langdon, C., Takahashi, T., Sweeney, C., Chipman, D., Atkinson, J. (2000). Rate of an experimental coral reef responds to manipulations in the concentrations of both CaCO3. Global Biogeochem. Cycles, 14, 639–654.

Lauvset, S. K., Gruber, N., Landschützer, P., Olsen, A., and Tjiputra, J.: Trends and drivers in global surface ocean pH over the past 3 decades. Biogeosciences, 12, 1285-1298, doi:10.5194/bg-12-1285-2015, 2015

Lazier, J., Hendry, R., Clarke, A., Yashayaev, I., Rhines, P. (2002). Convection and restratification in the Labrador Sea, 1990–2000. Deep Sea Res. Part I Oceanogr. Res. Pap., 49, 1819–1835. https://doi.org/10.1016/S0967-0637(02)00064-X

Lee, K., Kim, T.W., Byrne, R.H., Millero, F.J., Feely, R.A., Liu, Y.M. (2010). The universal ratio of boron to chlorinity for the North Pacific and North Atlantic oceans. Geochim. Cosmochim. Acta, 74, 1801–1811. https://doi.org/10.1016/j.gca.2009.12.027

Leseurre, C., Lo Monaco, C., Reverdin, G., Metzl, N., Fin, J., Olafsdottir, S., Racapé, V. (2020). Ocean carbonate system variability in the North Atlantic Subpolar surface water (1993–2017). Biogeosciences, 17, 2553–2577. https://doi.org/10.5194/bg-17-2553-2020

Lewis, E., Wallace, D. (1998). Program Developed for CO2 System Calculations ORNL/CDIAC-105, Carbon Dioxide Information Analysis Centre.

Lherminier, P., Mercier, H., Huck, T., Gourcuff, C., Perez, F. F., Morin, P., Sarafanov, A., and Falina, A. (2010). The Atlantic Meridional Overturning Circulation and the subpolar gyre observed at the A25-OVIDE section in June 2002 and 2004. Deep Sea Research Part I: Oceanographic Research Papers, 57(11), 1374-1391.

Lherminier, P., Perez, F. F., Branellec, P., Mercier, H., Velo, A., Messias, M. J., Castrillejo, M., Reverdin, G., Fontela, M., Baurand, F. (2022). GO-SHIP A25 - OVIDE 2018 Cruise data. SEANOE. https://doi.org/10.17882/87394

Lueker, T.J., Dickson, A.G., Keeling, C.D. (2000). Ocean pCO2 calculated from dissolved inorganic carbon, alkalinity, and equations for K1 and K2: Validation based on laboratory measurements of CO2 in gas and seawater at equilibrium. Mar. Chem., 70, 105–119. https://doi.org/10.1016/S0304-4203(00)00022-0

Marsh, R., de Cuevas, B.A., Coward, A.C., Bryden, H.L., Álvarez, M. (2005). Thermohaline circulation at three key sections in the North Atlantic over 1985–2002. Geophys. Res. Lett., 32, 1–4. https://doi.org/10.1029/2004GL022281

Matear, R.J., Lenton, A. (2014). Quantifying the impact of ocean acidification on our future climate. Biogeosciences, 11, 3965–3983. https://doi.org/10.5194/bg-11-3965-2014

Maier-Reimer, E., & Hasselmann, K. (1987). Transport and storage of CO2 in the ocean: an inorganic ocean-circulation carbon cycle model. Climate dynamics, 2, 63-90.

Maier, C., Hegeman, J., Weinbauer, M. G., & Gattuso, J. P. (2009). Calcification of the cold-water coral Lophelia pertusa, under ambient and reduced pH. Biogeosciences, 6(8), 1671-1680. https://doi.org/10.5194/bg-6-1671-2009

Mauritzen, C., Häkkinen, S. (1999). On the relationship between dense water formation and the "Meridional Overturning Cell" in the North Atlantic Ocean. Deep. Res. Part I Oceanogr. Res. Pap., 46, 877–894. https://doi.org/10.1016/S0967-0637(98)00094-6

McDonagh, E.L., King, B.A., Bryden, H.L., Courtois, P., Szuts, Z., Baringer, M., Cunningham, S.A., Atkinson, C., McCarthy, G. (2015). Continuous estimate of Atlantic oceanic freshwater flux at 26.5°N. Journal of Climate, 28, 8888–8906. https://doi.org/10.1175/JCLI-D-14-00519.1

McGrath, T., Kivimäe, C., McGovern, E., Cave, R.R., Joyce, E. (2013). Winter measurements of oceanic biogeochemical parameters in the Rockall Trough (2009-2012). Earth System Science Data, 5, 375–383. https://doi.org/10.5194/essd-5-375-2013

McGrath, T., Kivimäe, C., Tanhua, T., Cave, R.R., McGovern, E. (2012a). Inorganic carbon and pH levels in the Rockall Trough 1991-2010. Deep Sea Research Part I: Oceanographic Research Papers, 68, 79–91. https://doi.org/10.1016/j.dsr.2012.05.011

McGrath, T., Nolan, G., McGovern, E. (2012b). Chemical characteristics of water masses in the Rockall Trough. Deep Sea Research Part I: Oceanographic Research Papers, 61, 57–73. https://doi.org/10.1016/j.dsr.2011.11.007

McCartney, M. S., & Talley, L. D. (1982). The subpolar mode water of the North Atlantic Ocean. Journal of Physical Oceanography, 12(11), 1169-1188.

Mercier, H., Lherminier, P., Sarafanov, A., Gaillard, F., Daniault, N., Desbruyères, D., Falina, A., Ferron, B., Gourcuff, C., Huck, T., Thierry, V. (2015). Variability of the meridional overturning circulation at the Greenland – Portugal OVIDE section from 1993 to 2010. Progress in Oceanography, 132, 250–261. https://doi.org/10.1016/j.pocean.2013.11.001

Messias, M.J., Watson, A.J., Johannessen, T., Oliver, K.I.C., Olsson, K.A., Fogelqvist, E., Olafsson, J., Bacon, S., Balle, J., Bergman, N., Budéus, G., Danielsen, M., Gascard, J.C., Jeansson, E., Olafsdottir, S.R., Simonsen, K., Tanhua, T., Van Scoy, K., Ledwell, J.R. (2008). The Greenland Sea tracer experiment 1996–2002: Horizontal mixing and transport of Greenland Sea Intermediate Water. Progress in Oceanography, 78, 85–105. https://doi.org/10.1016/J.POCEAN.2007.06.005

Millero, F.J., Zhang, J., Lee, K., Campbell, D.M. (1993). Titration alkalinity of seawater. 44, 153–165.

Mintrop, L., Pérez, F.F., González-Dávila, M., Santana-Casiano, J.M., Körtzinger, A. (2000). Alkalinity determination by potentiometry: Intercalibration using three different methods. Ciencias Marinas, 26, 23–37. https://doi.org/10.7773/cm.v26i1.573

Moss, R. H., Edmonds, J. A., Hibbard, K. A., Manning, M. R., Rose, S. K., Van Vuuren, D. P., Carter, T. R., Emori, S., Kainuma, M., Kram, T., Meehl, G. A., Mitchell, J. F. B., Nakicenovic, N., Riahi, K., Smith, S. J., Stouffer, R. J., Thomson, A. M., Weyant, J. P., and Wilbanks, T. J. (2010). The next generation of scenarios for climate change research and assessment. *Nature*, *463*(7282), 747-756. https://doi.org/10.1038/nature08823

Mucci, A. (1983). The solubility of calcite and aragonite in seawater at various salinities, temperatures, and one atmosphere total pressure. American Journal of Science, 283(7), 780-799.

Olafsson, J., Olafsdottir, S.R., Benoit-Cattin, A., Danielsen, M., Arnarson, T.S., Takahashi, T. (2009). Rate of Iceland Sea acidification from time series measurements. Biogeosciences, 6, 2661–2668. https://doi.org/10.5194/bg-6-2661-2009

Olafsson, J., Olafsdottir, S.R., Benoit-Cattin, A., Takahashi, T. (2010). The Irminger Sea and the Iceland Sea time series measurements of seawater carbon and nutrient chemistry 1983-2008. Earth System Science Data, 2, 99–104. https://doi.org/10.5194/essd-2-99-2010

Orr, J.C., Epitalon, J.-M., Dickson, A. G., Gattuso, J.-P., (2018). Routine uncertainty propagation for the marine carbon dioxide system. Marine Chemistry 207, 84-107. https://doi.org/10.1016/j.marchem.2018.10.006

Orr, J.C., Fabry, V.J., Aumont, O., Bopp, L., Doney, S.C., Feely, R.A., Gnanadesikan, A., Gruber, N., Ishida, A., Joos, F., Key, R.M., Lindsay, K., Maier-Reimer, E., Matear, R., Monfray, P., Mouchet, A., Najjar, R.G., Plattner, G.K., Rodgers, K.B., Sabine, C.L., Sarmiento, J.L., Schlitzer, R., Slater, R.D., Totterdell, I.J., Weirig, M.F., Yamanaka, Y., Yool, A. (2005). Anthropogenic ocean acidification over the twenty-first century and its impact on calcifying organisms. Nature, 437, 681–686. [https://doi.org/10.1038/nature

Ostle C., P. Landschützer, M. Edwards, M. Johnson, S. Schmidtko, U. Schuster, A. J. Watson and C. Robinson, 2022. Multidecadal changes in biology influence the variability of the North Atlantic carbon sink. Environ. Res. Lett. 17, 114056, DOI : 10.1088/1748-9326/ac9ecf

Pérez, F.F., Fontela, M., García-Ibáñez, M.I., Mercier, H., Velo, A., Lherminier, P., Zunino, P., De La Paz, M., Alonso-Pérez, F., Guallart, E.F., Padin, X.A. (2018). Meridional overturning circulation conveys fast acidification to the deep Atlantic Ocean. Nature, 554, 515–518. https://doi.org/10.1038/nature25493

Pérez, F.F., Fraga, F. (1987). Association constant of fluoride and hydrogen ions in seawater. Marine Chemistry, 21, 161–168. https://doi.org/10.1016/0304-4203(87)90036-3

Pérez, F.F., Mercier, H., Vázquez-Rodríguez, M., Lherminier, P., Velo, A., Pardo, P.C., Rosón, G., Ríos, A.F. (2013). Atlantic Ocean CO2 uptake reduced by weakening of the meridional overturning circulation. Nature Geoscience, 6, 146–152. https://doi.org/10.1038/ngeo1680

Pérez, F.F., Olafsson, J., Ólafsdóttir, S.R., Fontela, M., Takahashi, T. (2021). Contrasting drivers and trends of ocean acidification in the subarctic Atlantic. Scientific Reports, 11, 1–16. https://doi.org/10.1038/s41598-021-93324-3

Pérez, F.F., Vázquez-Rodríguez, M., Louarn, E., Padín, X.A., Mercier, H., Ríos, A.F. (2008). Temporal variability of the anthropogenic CO2 storage in the Irminger Sea. Biogeosciences, 5, 1669–1679. https://doi.org/10.5194/bg-5-1669-2008

Pérez, F.F., Vázquez-Rodríguez, M., Mercier, H., Velo, A., Lherminier, P., Ríos, A.F. (2010). Trends of anthropogenic CO2 storage in North Atlantic water masses. Biogeosciences, 7, 1789–1807. https://doi.org/10.5194/bg-7-1789-2010

Perez, F. F., Becker, M., Goris, N., Gehlen, M., Lopez-Mozos, M., Tjiputra, J., Olsen, A., Müller, J. D., Huertas, I. E., Chau, T. T. T., Cainzos, V., Velo, A., Benard, G., Hauck, J., Gruber, N., Wanninkhof, R. (2024). An assessment of CO2 storage and sea-air fluxes for the Atlantic Ocean and Mediterranean Sea between 1985 and 2018. Global Biogeochemical Cycles, 38, e2023GB007862. https://doi.org/10.1029/2023GB007862

Pickart, R.S., Spall, M.A., Ribergaard, M.H., Moore, G.W.K., Milliff, R.F. (2003). Deep convection in the Irminger Sea forced by the Greenland tip jet. Nature, 424, 152–156. https://doi.org/10.1038/nature01729

Piron, A., Thierry, V., Mercier, H., Caniaux, G. (2017). Gyre-scale deep convection in the subpolar North Atlantic Ocean during winter 2014–2015. Geophysical Research Letters, 44, 1439–1447. https://doi.org/10.1002/2016GL071895

Pollard, R.T., Griffiths, M.J., Cunningham, S.A., Read, J.F., Pérez, F.F., Ríos, A.F. (1996). Vivaldi 1991 - A study of the formation, circulation, and ventilation of Eastern North Atlantic Central Water. Progress in Oceanography, 37, 167–172. https://doi.org/10.1016/S0079-6611(96)00008-0

Portner, H.O., Langenbuch, M., & Reipschläger, A. (2004). Biological Impact of Elevated Ocean CO2 Concentrations: Lessons from Animal Physiology and Earth History. Journal of Oceanography, 60, 705–718.

Pörtner, H. O., et al. (2019). IPCC Special Report on the Ocean and Cryosphere in a Changing Climate. Wiley IPCC Intergovernmental Panel on Climate Change.

Ramette, R.W., Culberson, C.H., and Bates, R.G. (1977). Acid-base properties of tris(hydroxymethyl) aminomethane (tris) buffers in seawater from 5 to 40°C. Analytical Chemistry 49, 867—870. https://doi.org/10.1021/ac50014a049

Raven, J., Caldeira, K., Elderfield, H., Hoegh-Guldberg, O., Liss, P., Riebesell, U., Shepherd, J., Turley, C., & Watson, A. (2005). Ocean acidification due to increasing. Coral Reefs, 12/05, 68.

Read, J.F. (2000). CONVEX-91: Water masses and circulation of the Northeast Atlantic subpolar gyre. Progress in Oceanography, 48, 461–510. https://doi.org/10.1016/S0079-6611(01)00011-8

Riebesell, U., Zondervan, I., Rost, B., Tortell, P.D., Zeebe, R.E., Morel, F.M.M. (2000). Reduced calcification of marine plankton in response to increased atmospheric CO2. Nature, 407, 364–366. https://doi.org/10.1038/35030078

Ríos, A.F., Resplandy, L., García-Ibáñez, M.I., Fajar, N.M., Velo, A., Padin, X.A., Wanninkhof, R., Steinfeldt, R., Rosón, G., Pérez, F.F., Morel, F.M.M. (2015). Decadal acidification in the water masses of the Atlantic Ocean. Proceedings of the National Academy of Sciences, U.S.A., 112, 9950–9955. https://doi.org/10.1073/pnas.1504613112

Roberts, J.M., Wheeler, A.J., Freiwald, A., Cairns, S. (2009). Cold-Water Corals: The Biology and Geology of Deep-Sea Coral Habitats. Cambridge University Press. https://doi.org/10.1017/CBO9780511581588.

Robson, J., Hodson, D., Hawkins, E., Sutton, R. (2014). Atlantic overturning in decline? Nature Geoscience, 7, 2–3. https://doi.org/10.1038/ngeo2050

Robson, J., Ortega, P., Sutton, R. (2016). A reversal of climatic trends in the North Atlantic since 2005. Nature Geoscience, 9, 513–517. https://doi.org/10.1038/ngeo2727

Rodgers, K.B., Key, R.M., Gnanadesikan, A., Sarmiento, J.L., Aumont, O., Bopp, L., Doney, S.C., Dunne, J.R., Glover, D.M., Ishida, A., Ishii, M., Jacobson, A.R., Monaco, C. Lo, Maier-Reimer, E., Mercier, H., Metzl, N., Pérez, F.F., Rios, A.F., Wanninkhof, R., Wetzel, P., Winn, C.D., Yamanaka, Y. (2009). Using altimetry to help explain patchy changes in hydrographic carbon measurements. Journal of Geophysical Research: Ocean, 114, 1–20. https://doi.org/10.1029/2008JC005183

Sabine, C.L., Feely, R.A., Gruber, N., Key, R.M., Lee, K., Bullister, J.L., Wanninkhof, R., Wong, C.S., Wallace, D.W.R., Tilbrook, B., Millero, F.J., Peng, T.H., Kozyr, A., Ono, T., Rios, A.F. (2004a). The oceanic sink for anthropogenic CO2. Science, 305, 367–371. https://doi.org/10.1126/science.1097403

Sabine, C.L., Feely, R.A., Gruber, N., Key, R.M., Lee, K., Bullister, J.L., Wanninkhof, R., Wong, C.S., Wallace, D.W.R., Tilbrook, B., Millero, F.J., Peng, T.H., Kozyr, A., Ono, T., Rios, A.F. (2004b). The oceanic sink for anthropogenic CO2. Science, 305, 367–371. https://doi.org/10.1126/SCIENCE.1097403/SUPPL_FILE/SABINE.SOM.PDF

Santana-Casiano, J. M., González-Dávila, M., and Curbelo-Hernández, D. (2023). Surface-to-bottom data of total alkalinity, total inorganic carbon, pH and dissolved oxygen in the subpolar North Atlantic along the CLIVAR 59.5N hydrographic section during 2009-2019. [Data set]. Zenodo. https://doi.org/10.5281/zenodo.10276222

Santana-Casiano, J.M., González-Dávila, M., Rueda, M.-J., Llinás, O., González-Dávila, E.-F. (2007). The interannual variability of oceanic CO2 parameters in the northeast Atlantic subtropical gyre at the ESTOC site. Global Biogeochemical Cycles, 21. https://doi.org/10.1029/2006GB002788

Sarafanov, A., Falina, A., Mercier, H., Sokov, A., Lherminier, P., Gourcuff, C., Gladyshev, S., Gaillard, F., and Daniault, N. (2012). Mean full-depth summer circulation and transports

at the northern periphery of the Atlantic Ocean in the 2000s. Journal of Geophysical Research: Oceans, 117(C1).

Sarafanov, A., Falina, A., Sokov, A., Zapotylko, V., Gladyshev, S. (2018). Ship-Based Monitoring of the Northern North Atlantic Ocean by the Shirshov Institute of Oceanology. The Main Results. In: Velarde, M., Tarakanov, R., Marchenko, A. (eds) The Ocean in Motion. Springer Oceanography. Springer, Cham. https://doi.org/10.1007/978-3-319-71934-4_25

Sarafanov, A., Mercier, H., Falina, A., and Sokov, A. (2010). Cessation and partial reversal of deep water freshening in the northern North Atlantic: observation-based estimates and attribution. Tellus A: Dynamic Meteorology and Oceanography, 62:1, 80-90. https://doi.org/10.1111/j.1600-0870.2009.00418.x

Sarmiento, J.L., Orr, J.C., Siegenthaler, U. (1992). A perturbation simulation of CO2 uptake in an ocean general circulation model. Journal of Geophysical Research: Ocean, 97, 3621–3645. https://doi.org/10.1029/91JC02849

Saunders, P. M., (2001). Chapter 5.6 The dense northern overflows. Int. Geophys., 77, 401–417. https://doi.org/10.1016/S0074-6142(01)80131-5

Sauzède, R., Bittig, H.C., Claustre, H., de Fommervault, O.P., Gattuso, J.P., Legendre, L., Johnson, K.S. (2017). Estimates of water-column nutrient concentrations and carbonate system parameters in the global ocean: A novel approach based on neural networks. Frontiers in Marine Science, 4, 1–17. https://doi.org/10.3389/fmars.2017.00128

Schlitzer, R. (2021). Ocean Data View. Available at: https://odv.awi.de.

Schmitz Jr, W. J., & McCartney, M. S. (1993). On the north Atlantic circulation. Reviews of Geophysics, 31(1), 29-49.

Schott, F. A., & Brandt, P. (2007). Circulation and deep water export of the subpolar North Atlantic during the 1990's. Washington DC American Geophysical Union Geophysical Monograph Series, 173, 91-118.

Sharp, J.D., Pierrot, D., Humphreys, M.P., Epitalon, J.-M., Orr, J.C., Lewis, E.R., Wallace, D.W.R. (2023, Jan. 19). CO2SYSv3 for MATLAB (Version v3.2.1). Zenodo. http://doi.org/10.5281/zenodo.3950562

Smeed, D.A., Josey, S.A., Beaulieu, C., Johns, W.E., Moat, B.I., Frajka-Williams, E., Rayner, D., Meinen, C.S., Baringer, M.O., Bryden, H.L., McCarthy, G.D. (2018). The North Atlantic Ocean Is in a State of Reduced Overturning. Geophysical Research Letters, 45, 1527–1533. https://doi.org/10.1002/2017GL076350

Steinfeldt, R., Rhein, M., Bullister, J.L., Tanhua, T. (2009). Inventory changes in anthropogenic carbon from 1997 – 2003 in the Atlantic Ocean between 20 ° S and 65 ° N, 23, 1–11. https://doi.org/10.1029/2008GB003311

Stephens, T. (2021). Ocean Acidification. In: Research Handbook on Law, Governance and the Planetary Boundaries. 22, 295–308. https://doi.org/10.4337/9781789902747.00025

Stramma, L., Kieke, D., Rhein, M., Schott, F., Yashayaev, I., Koltermann, K.P. (2004). Deep water changes at the western boundary of the subpolar North Atlantic during 1996 to 2001. Deep Sea Research Part I: Oceanographic Research Papers, 51, 1033–1056. https://doi.org/10.1016/J.DSR.2004.04.001

Sutherland, D. A., and Pickart, R. S. (2008). The East Greenland coastal current: Structure, variability, and forcing. Progress in Oceanography, 78(1), 58-77.

Takahashi, T., Olafsson, J., Goddard, J.G., Chipman, D.W., Sutherland, S.C. (1993). Seasonal variation of CO2 and nutrients in the high-latitude surface oceans: A comparative study. Global Biogeochemical Cycles, 7, 843–878. https://doi.org/10.1029/93GB02263

Takahashi, T., Sutherland, S.C., Wanninkhof, R., Sweeney, C., Feely, R.A., Chipman, D.W., Hales, B., Friederich, G., Chavez, F., Sabine, C., Watson, A., Bakker, D.C.E., Schuster, U., Metzl, N., Yoshikawa-Inoue, H., Ishii, M., Midorikawa, T., Nojiri, Y., Körtzinger, A., Steinhoff, T., Hoppema, M., Olafsson, J., Arnarson, T.S., Tilbrook, B., Johannessen, T., Olsen, A., Bellerby, R., Wong, C.S., Delille, B., Bates, N.R., de Baar, H.J.W. (2009). Climatological mean and decadal change in surface ocean pCO2, and net sea-air CO2 flux over the global oceans. Deep Sea Research Part II: Topical Studies in Oceanography, 56, 554–577. https://doi.org/10.1016/j.dsr2.2008.12.009

Tanhua, T., Körtzinger, A., Friis, K., Waugh, D.W., Wallace, D.W.R. (2007). An estimate of anthropogenic CO2 inventory from decadal changes in oceanic carbon content. Proceedings of the National Academy of Sciences, U.S.A., 104, 3037–3042. https://doi.org/10.1073/pnas.0606574104

Tesdal, J.E., Abernathey, R.P., Goes, J.I., Gordon, A.L., Haine, T.W.N. (2018). Salinity trends within the upper layers of the subpolar North Atlantic. Journal of Climate, 31, 2675–2698. https://doi.org/10.1175/JCLI-D-17-0532.1

Thomas, H., Prowe, A.E.F., Lima, I.D., Doney, S.C., Wanninkhof, R., Greatbatch, R.J., Schuster, U., Corbière, A. (2008). Changes in the North Atlantic Oscillation influence CO2 uptake in the North Atlantic over the past 2 decades. Global Biogeochemical Cycles, 22, 1–13. https://doi.org/10.1029/2007GB003167

Tjiputra, J.F., Olsen, A., Bopp, L., Lenton, A., Pfeil, B., Roy, T., Segschneider, J., Totterdell, I., Heinze, C. (2014). Long-term surface pCO2 trends from observations and models. Tellus, Series B: Chemical and Physical Meteorology, 66, 1–24. https://doi.org/10.3402/tellusb.v66.23083

Touratier, F., Azouzi, L., Goyet, C. (2007). CFC-11, Δ14C and 3H tracers as a means to assess anthropogenic CO2 concentrations in the ocean. Tellus, Series B: Chemical and Physical Meteorology, 59, 318–325. https://doi.org/10.1111/j.1600-0889.2006.00247.x

Tsuchiya, M., Talley, L.D., McCartney, M.S. (1992). An eastern Atlantic section from Iceland southward across the equator. Deep Sea Research Part A: Oceanographic Research Papers, 39, 1885–1917. https://doi.org/10.1016/0198-0149(92)90004-D

Urban-Rich, J., Dagg, M., Peterson, J. (2001). Copepod grazing on phytoplankton in the Pacific sector of the Antarctic polar front. Deep Sea Research Part II: Topical Studies in Oceanography, 48, 4223–4246. https://doi.org/10.1016/S0967-0645(01)00087-X

Våge, K., Pickart, R.S., Thierry, V., Reverdin, G., Lee, C.M., Petrie, B., Agnew, T.A., Wong, A., Ribergaard, M.H. (2009). Surprising return of deep convection to the subpolar North Atlantic Ocean in winter 2007-2008. Nature Geoscience, 2, 67–72. https://doi.org/10.1038/ngeo382

Van Aken, H.M., and Becker, G. (1996). Hydrography and through-flow in the north-eastern North Atlantic Ocean: the NANSEN project. Prog. Oceanogr. 38, 297–346. https://doi.org/10.1016/S0079-6611(97)00005-0

Van Aken, H. M., and De Boer, C. J. (1995). On the synoptic hydrography of intermediate and deep water masses in the Iceland Basin. Deep Sea Research Part I: Oceanographic Research Papers, 42(2), 165-189.

Van Heuven, S., D. Pierrot, J.W.B. Rae, E. Lewis, and D.W.R. Wallace (2011). MATLAB Program Developed for CO2 System Calculations. ORNL/CDIAC-105b. Carbon Dioxide Information Analysis Center, Oak Ridge National Laboratory, U.S. Department of Energy, Oak Ridge, Tennessee. https://doi.org/10.3334/CDIAC/otg.CO2SYS_MATLAB_v1.1

Van Vuuren, D. P., Edmonds, J., Kainuma, M., Riahi, K., Thomson, A., Hibbard, K., Hurtt, G. C., Kram, T., Krey, V., Lamarque, J-F., Masui, T., Meinshausen, M., Nakicenovic, N., Smith, S. J., and Rose, S. K. (2011). The representative concentration pathways: an overview. *Climatic change*, *109*, 5-31. https://doi.org/10.1007/s10584-011-0148-z

Vázquez-Rodríguez, M., Padin, X.A., Pardo, P.C., Ríos, A.F., Pérez, F.F. (2012). The subsurface layer reference to calculate preformed alkalinity and air-sea CO2 disequilibrium in the Atlantic Ocean. J. Mar. Syst. 94, 52–63. https://doi.org/10.1016/j.jmarsys.2011.10.008

Vázquez-Rodríguez, M., Pérez, F.F., Velo, A., Ríos, A.F., Mercier, H. (2012). Observed acidification trends in North Atlantic water masses. Biogeosciences 9, 5217–5230. https://doi.org/10.5194/bg-9-5217-2012

Vázquez-Rodríguez, M., Touratier, F., Monaco, C. Lo, Waugh, D.W., Padin, X.A., Bellerby, R.G.J., Goyet, C., Metzl, N., Ríos, A.F., Pérez, F.F. (2009). Anthropogenic carbon distributions in the Atlantic Ocean: Data-based estimates from the Arctic to the Antarctic. Biogeosciences 6, 439–451. https://doi.org/10.5194/BG-6-439-2009

Wallace, D. W. (2001). Storage and transport of excess CO2 in the oceans: The JGOFS/WOCE global CO2 survey. In International Geophysics (Vol. 77, pp. 489-L). Academic Press. https://doi.org/10.1016/S0074-6142(01)80136-4

Watson, A.J., Schuster, U., Bakker, D.C.E., Bates, N.R., Corbière, A., González-Davila, M., Friedrich, T., Hauck, J., Heinze, C., Johannessen, T., Körtzinger, A., Metzl, N., Olafsson, J., Olsen, A., Oschlies, A., Antonio Padin, X., Pfeil, B., Magdalena Santana-Casiano, J., Steinhoff, T., Telszewski, M., Rios, A.F., Wallace, D.W.R., Wanninkhof, R. (2009). Tracking the variable North Atlantic sink for atmospheric CO2. Science (80-. ). 326, 1391–1393. https://doi.org/10.1126/science.1177394

Winkler, L. W. (1888). Die bestimmung des im wasser gelösten sauerstoffes. Berichte der deutschen chemischen Gesellschaft, 21(2), 2843-2854.

Xu, X., Hurlburt, H.E., Jr, W.J.S., Zantopp, R., Fischer, J., Hogan, P.J. (2013). On the currents and transports connected with the atlantic meridional overturning circulation in the subpolar North Atlantic. J. Geophys. Res. 118, 502–516. https://doi.org/10.1002/jgrc.20065

Yashayaev, I. (2007). Hydrographic changes in the Labrador Sea, 1960–2005. Progress in Oceanography, 73(3-4), 242-276. https://doi.org/10.1016/j.pocean.2007.04.015

Yashayaev, I., Dickson, B. (2008). Transformation and Fate of Overflows in the Northern North Atlantic. In: Dickson, R.R., Meincke, J., Rhines, P. (eds) Arctic–Subarctic Ocean Fluxes. Springer, Dordrecht. https://doi.org/10.1007/978-1-4020-6774-7_22

Yashayaev, I., Holliday, N. P., Bersch, M., and van Aken, H. M. (2008). The history of the Labrador Sea Water: Production, spreading, transformation and loss. Arctic–Subarctic Ocean Fluxes: Defining the Role of the Northern Seas in Climate, 569-612.

Yashayaev, I., Lazier, J., & Clarke, R. (2003). Temperature and salinity in the central Labrador Sea during the 1990s and in the context of the longer-term change. Retrieved from https://doi.org/10.17895/ices.pub.19271729